DISEASE-SPECIFIC BRAIN ATLASES

[1]Paul M. Thompson, [1,2]Michael S. Mega, and [1]Arthur W. Toga

[1]Laboratory of Neuro Imaging, and [2]Alzheimer's Disease Center,
Dept. of Neurology, Division of Brain Mapping
UCLA School of Medicine, Los Angeles, CA

A Book Chapter for:

Brain Mapping III: The Disorders
John C. Mazziotta and Arthur W. Toga, Editors
Academic Press

Please address correspondence to:
Dr. Paul Thompson
(Rm. 4238, Reed Neurological Research Center)
Laboratory of Neuro Imaging, Dept. of Neurology, UCLA School of Medicine
710 Westwood Plaza, Los Angeles, CA 90095-1769
Phone: (310) 206-2101 **Fax:** (310) 206-5518 **E-mail:** thompson@loni.ucla.edu

Acknowledgments:
This work was supported by research grants from the National Center for Research Resources (P41 RR13642 and RR05956), the National Institute of Neurological Disorders and Stroke and the National Institute of Mental Health (NINDS/NIMH NS38753), and by a *Human Brain Project* grant to the International Consortium for Brain Mapping, funded jointly by NIMH and NIDA (P20 MH/DA52176). Additional support was also provided by the United States Information Agency (Grant G-1-00001), Howard Hughes Medical Institute, and U.S.-U.K. Fulbright Commission (to P.T.), and by the National Library of Medicine (LM/MH05639) and National Science Foundation (BIR 93-22434). Special thanks go to our colleagues Roger Woods, Colin Holmes, Jay Giedd, David MacDonald, Alan Evans, and John Mazziotta, whose advice and support have been invaluable in these investigations.

DISEASE-SPECIFIC BRAIN ATLASES

[1]Paul M. Thompson, [1,2]Michael S. Mega, and [1]Arthur W. Toga

[1]Laboratory of Neuro Imaging, and [2]Alzheimer's Disease Center,
Dept. of Neurology, Division of Brain Mapping,
UCLA School of Medicine, Los Angeles, CA

CONTENTS

DISEASE-SPECIFIC BRAIN ATLASES

[1]Paul M. Thompson, [1,2]Michael S. Mega, and [1]Arthur W. Toga

[1]Laboratory of Neuro Imaging, and [2]Alzheimer's Disease Center,
Dept. of Neurology, Division of Brain Mapping,
UCLA School of Medicine, Los Angeles, CA

I. Challenges in Population-Based Brain Mapping

Advanced brain imaging technologies now provide a means to investigate disease and therapeutic response in their full spatial and temporal complexity. Imaging studies of clinical populations continue to uncover new patterns of altered structure and function, and novel algorithms are being applied to relate these patterns to cognitive and genetic parameters. Post mortem brain maps are also beginning to clarify the molecular substrates of disease.

As imaging studies expand into ever-larger patient populations, population-based brain atlases offer a powerful framework to synthesize the results of disparate imaging studies. These atlases use novel analytical tools to fuse data across subjects, modalities, and time. They detect group-specific features not apparent in individual patients' scans. Once built, these atlases can be stratified into subpopulations to reflect a particular clinical group. The disease-specific features they resolve can then be linked with demographic factors such as age, gender, handedness, as well as specific clinical or genetic parameters (Mazziotta et al., 1995; Toga and Mazziotta, 1996).

New brain atlases are also being built to incorporate dynamic data. Despite the significant challenges in expanding the atlas concept to the time dimension, dynamic brain atlases are beginning to include probabilistic information on growth rates that may assist research into pediatric disorders (Thompson and Toga, 1999). Imaging algorithms are also significantly improving the flexibility of digital brain templates. *Deformable brain atlases* are adaptable brain templates that can be individualized to reflect the anatomy of new subjects, and *probabilistic atlases* are research tools that retain information on cross-subject variations in brain structure and function. These atlases are powerful new tools with broad clinical and research applications (Roland and Zilles, 1994; Kikinis et al., 1996; Toga and Thompson, 1998).

Disease-Specific Atlases. This chapter introduces the topic of a *disease-specific* brain atlas (Fig. 1). This type of atlas is designed to reflect the unique anatomy and physiology of a particular clinical subpopulation (Thompson et al., 1997, 1998, 1999; Mega et al., 1997, 1998, 1999; Narr et al., 1999). Based on well-characterized patient groups, these atlases contain thousands of structure models, as well as composite maps, average templates, and visualizations of structural variability, asymmetry and group-specific differences. They act as a quantitative framework that correlates the structural, metabolic, molecular and histologic hallmarks of the disease (Mega et al., 1997). Additional algorithms are described that use information stored in the atlas to recognize anomalies and label structures in new patients. Because they retain information on group anatomical variability, disease-specific atlases are a type of probabilistic atlas specialized to represent a particular clinical group. The resulting atlases can identify patterns of altered structure or function, and can guide algorithms for knowledge-based image analysis, automated image labeling (Collins et al., 1994; Pitiot et al., 1999), tissue classification (Zijdenbos and Dawant, 1994) and functional image analysis (Dinov et al., 1999).

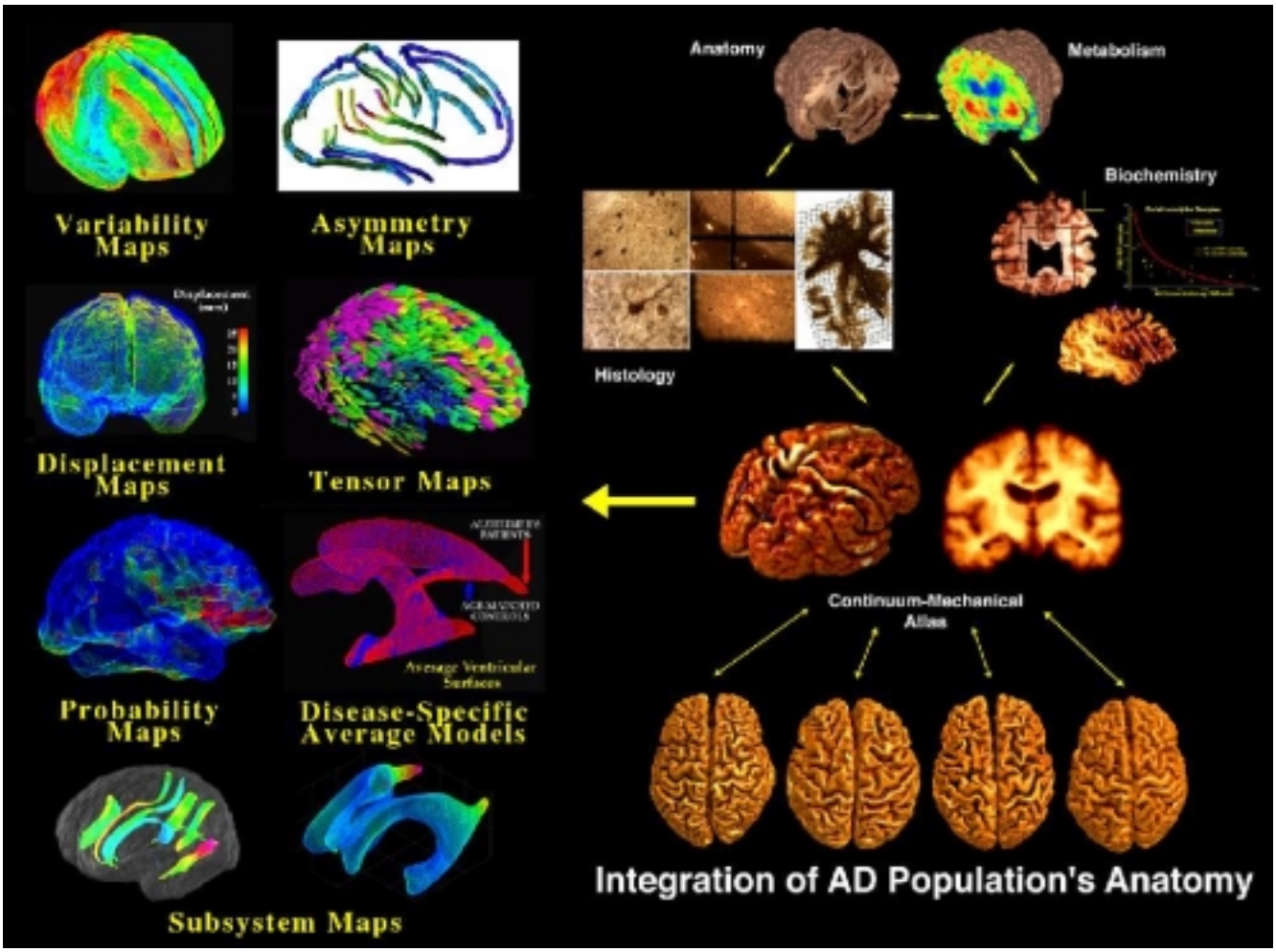

Fig. 1. *Elements of a Disease-Specific Atlas.* This schematic shows the types of maps and models contained in a disease-specific brain atlas. In the main text, we explain how these maps are created, and review their applications. Examples are shown from an atlas that represents an Alzheimer's Disease population. To construct the atlas, databases of structural imaging data are used to develop detailed models of cortical structure and anatomic subsystems. These models are statistically combined to create group average models that can be compared with a normal database. Patterns of variability, asymmetry, and disease-specific differences are also computed from the anatomic data. Specialized techniques create a well-resolved average image template for the patient population (Continuum-Mechanical Template, *center right*). This template provides a coordinate framework to link *in vivo* metabolic and functional data with fine-scale anatomy and biochemistry. In recent studies (Mega et al., 1997), histologic maps of *post mortem* neurofibrillary tangle (NFT) staining density were correlated with *in vivo* metabolism. 3D FDG-PET data, obtained 8 hours before death, was compared with whole-brain cryosections acquired immediately *post mortem* and stained for NFTs by the Gallyas method. Using the algorithm of (Thompson and Toga, 1996; *warped image*), distorted tissue sections were elastically warped back to their configuration in the cryosection blockface (*top row*). A further 3D registration projected the data into pre-mortem MR and co-registered PET data (*top right*).

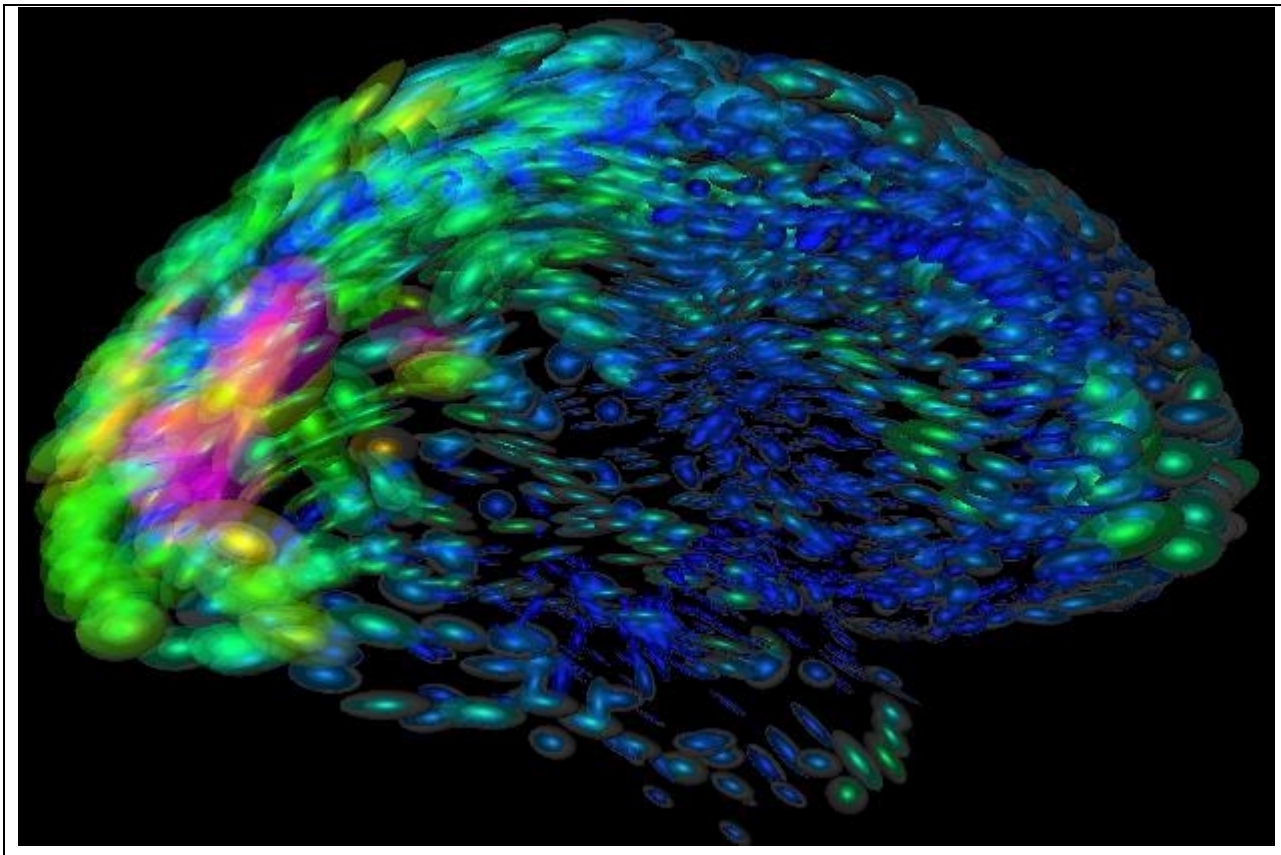

Panel 1. Disease-specific atlases can contain probabilistic information on how brain structure varies in large human populations (for detailed explanations of these atlasing approaches, please see Thompson et al., 1999). This *tensor map* reveals the preferred directions of cortical variation, after sulcal pattern correspondences are taken into account. Variability is greatest in temporo-parietal cortex. If cortical variations are modeled as vector field displacements of an average cortical model, ellipsoids of constant probability density can be computed for positions of cortical regions (relative to the average cortex). These ellipsoids are shown, colored by the determinant of the covariance tensor. Fields of tumbling ellipses have also been used to visualize multi-directional parameters in diffusion imaging data, and offer a means to represent cortical variability for anomaly detection and Bayesian image labeling.

We present data from several on-going projects, whose goal is to create disease-specific atlases of the brain in Alzheimer's Disease, schizophrenia, and several neurodevelopmental disorders. Since current brain templates poorly represent the anatomy of these clinical populations, the resulting atlases offer a framework to investigate each disease. Pathological change can be tracked over time, and disease-specific features resolved. Rather than simply fusing information from multiple subjects and sources, new mathematical strategies are introduced to resolve group-specific features not apparent in individual scans.

Anatomical Templates. Central to the construction of a disease-specific atlas is the creation of averages, templates and models to describe how the brain and its component parts are organized, and how they are altered in disease. Statistical models are created to reveal how major anatomic systems are affected, how the pathology progresses, and how these changes relate to demographic or genetic factors. To create templates that reflect the morphology of a diseased group, specialized strategies are required for population-based averaging of anatomy

(Thompson et al., 1996a,b, 1998; Grenander and Miller, 1998). In one approach (Thompson et al., 1999), sets of high-dimensional elastic mappings, based on the principles of continuum mechanics, reconfigure the anatomy of a large number of subjects in an anatomic image database. These three-dimensional deformation fields are used to create a crisp anatomical image template with highly-resolved structures in their mean spatial location. The mappings also generate a richly detailed local encoding of anatomic variability, with up to a billion parameters (Thompson and Toga, 1997; Grenander and Miller, 1998). The resulting variability parameters are stored as a tensor field (Section 9) and leveraged by pattern recognition strategies that automatically identify anatomical structures in new patients' scans, and identify disease-specific characteristics (Pitiot et al., 1999; Thompson et al., 1999).

Cortical Patterns. Cortical patterns are altered in a variety of diseases. Sulcal pattern anomalies have been identified in schizophrenia and epilepsy (Kikinis et al., 1994; Cook et al., 1994; Fuh et al., 1998), and diffuse cortical atrophy is typical of Alzheimer's disease, Pick's disease and other dementias (Schmidt, 1992). Gyral anomalies, such as cortical dysplasias, have also been linked with neurodevelopmental delay (Sobire et al., 1995). Nonetheless, ratings of structural change in the cortex are still largely based on qualitative assessment (Berg et al., 1993).

To clarify how diseases affect the cortex, specialized approaches are described for averaging cortical anatomy across subjects. Gyral pattern matching (Thompson and Toga, 1996; Thompson et al., 1999) is used to create average cortical models, to measure cross-subject differences, and to encode the magnitude and principal directions of anatomical variation at the cortex. In the resulting cortical templates, subtle features emerge. Regional asymmetries appear that are not apparent in individual anatomies. Population-based maps of cortical variation reveal a mosaic of variability patterns that are characteristic of each cortical region.

Pathology Detection. Normal anatomic complexity makes it difficult to design automated strategies that detect abnormal brain structure. Considerable research has focused on uncovering specific patterns of anatomic alterations in Alzheimer's Disease and other dementias (Friedland and Luxenberg, 1988), schizophrenia (Kikinis et al., 1994; Csernansky et al., 1998), epilepsy (Cook et al., 1994), attention deficit hyperactivity disorder (ADHD; Giedd et al., 1994), autism (Filipek et al., 1996; Courchesne, 1997), and cortical dysplasias (Sobire et al., 1995). Some of the results of these morphometric studies are summarized in Table 1. At the same time, brain structure is so variable that group-specific patterns of anatomy and function are often obscured.

Demographic Factors. Reports of structural differences in the brain linked to gender and handedness are still controversial, and these factors may also interact with disease-specific abnormalities (Thompson et al., 1999; Narr et al., 1999). Other factors that interfere with analysis include educational level, premorbid adjustment, treatment history and response, and the duration and course of illness (Carpenter et al., 1993). Interactions of these variables make it harder to detect disease-specific patterns and relate them to clinical and genetic parameters.

The importance of these linkages has propelled computational anatomy to the forefront of brain imaging investigations. To distinguish abnormalities from normal variants, a realistically complex mathematical framework is required to encode information on anatomic variability in homogeneous populations (Grenander and Miller, 1998; Thompson and Toga, 1999). As we shall see, elastic registration or *warping* algorithms offer substantial advantages in creating brain atlases that encode patterns of anatomic variation and detect pathology.

Dynamic Brain Atlases. While brain atlases have traditionally relied on static representations of anatomy, many of the diseases that affect the human brain are progressive (e.g., dementia, neoplastic tumors). Other disorders may be relapsing-remitting (e.g., multiple sclerosis), or may display a normal phenotype with an

aberrant time-course (e.g., delayed neurodevelopment). The progression of a disease may also be modulated by therapy, ranging from drug treatment to surgery. In response to these challenges, *dynamic* brain atlases retain spatio-temporal information on patterns of neuroanatomic change. They offer a means to analyze the dynamics of disease. Later in the chapter, we describe how atlases can be expanded to incorporate quantitative (4D) maps of growth or degenerative patterns in the brain. These maps characterize local growth or atrophic rates in development or disease. Atlases that incorporate confidence limits on growth rates, in particular, offer a new type of normative framework to analyze aberrant brain development and childhood onset disorders (Thompson and Toga, 1999).

II. Types of Brain Atlases

Coordinate Systems. Rapid progress has been made in recent years by research groups developing standardized three-dimensional brain atlases (Talairach and Tournoux, 1988; Greitz *et al*., 1991; Höhne *et al*., 1992; Thurfjell *et al*., 1993; Kikinis *et al*., 1996). While few of these atlases aim to represent anatomy and function in disease, several commercially-available atlases of pathology combine histologic data with illustrative metabolic or structural images. The *Harvard Brain Atlas* (Johnson et al., 1996) is a rich source of annotated CT, MRI, SPECT and PET (single photon/positron emission computed tomography) images from a number of clinical populations. Cerebrovascular, neoplastic and degenerative diseases are represented (including stroke, vascular dementia, and Alzheimer's Disease), as are inflammatory, autoimmune and infectious diseases (multiple sclerosis and AIDS). In a similar effort, the *Atlas of Brain Perfusion SPECT* has been produced by Brigham and Women's Hospital (Holman et al., 1994). This atlas presents 21 SPECT images with co-registered scans (SPECT merged with CT or MRI), and all scans are annotated with relevant clinical information and case histories. Other collections focus on post mortem data. The *On-line Neuropathology Atlas* developed by the University of Debrecen Medical School (Hegedüs and Molnár, 1996) includes labeled images of the normal brain, with an extensive collection of pathological images from patients with cerebrovascular disease, neoplasms, as well as inflammatory and degenerative disorders.

Perhaps surprisingly, few atlases of neuropathology use a standardized 3-dimensional coordinate system to integrate data across patients, techniques, and acquisitions. To suggest why this can be advantageous, we review recent developments in the brain atlasing field that have created a framework for inter-laboratory communication. Digital templates placed in a well-defined coordinate space (Evans et al., 1992; Friston et al., 1995; Drury and Van Essen, 1997), together with algorithms to align data with them (Toga, 1998), have enabled the pooling of brain mapping data from multiple subjects and sources, including large patient populations. As we shall see, standardized coordinate systems also allow parameterized, anatomical models to be statistically combined (Thompson et al., 1996). By combining anatomical models, the results of morphometric studies can be leveraged to create disease-specific brain templates. Automated algorithms can then capitalize on atlas descriptions of anatomical variance to guide image segmentation (Le Goualher, 1998; Pitiot et al., 1999), tissue classification (Zijdenbos and Dawant, 1994), functional image analysis (Dinov et al., 1999) and pathology detection (Thompson et al., 1997).

Before describing atlases specialized to represent disease, we first review developments in informatics that led to the creation of deformable anatomic templates. These templates are a flexible type of brain atlas that can be customized to represent a given individual, and then subsequently to represent a population.

Early Anatomic Templates. Research on brain atlases was originally based on the premise that brain structure and function imaged in any modality can be better localized by correlation with higher resolution anatomic data placed in an appropriate spatial coordinate system. Three-dimensional brain templates also provide reference information for surgical planning, and have been used to guide stereotaxic radiosurgery and electrode

implantations (Talairach et al., 1967; Kikinis et al., 1996). Because of their detailed characterization of anatomy, most early brain atlases were derived from one, or a few, *post mortem* specimens (Brodmann, 1909; Schaltenbrand and Bailey, 1959; Van Buren and Maccubin, 1962; Talairach et al., 1967; Van Buren and Borke, 1972; Schaltenbrand and Wahren, 1977; Matsui and Hirano, 1978; Talairach and Tournoux, 1988; Ono et al., 1990). These anatomical references typically represent a particular feature of the brain, such as a neurochemical distribution (Mansour et al., 1995), myelination patterns (Smith, 1907; Mai et al., 1997), or the cellular architecture of the cortex (Brodmann, 1909).

Digital Manipulations. Atlas templates became considerably easier to manipulate with the transition from paper to digital format. Widely-used brain atlases were converted to electronic form, and image registration algorithms made it feasible to overlay digital atlas data onto volumetric radiologic scans. In an endeavor to fuse data from multiple atlases, Nowinski et al. (1997) merged the thalamic and brainstem anatomical maps of Schaltenbrand and Wahren (1977), and the Talairach atlases (1988) with cortical and sulcal atlases employed in radiology (Brodmann, 1909; Ono et al., 1990). Recent neurosurgical systems (e.g., the CASS system; Computer Assisted Stereotaxic Surgery, Midco Corporation, CA) now support the digital overlay of the Schaltenbrand, Talairach and Brodmann atlas data onto individual patient MR scans to create composite maps and simulation displays for surgical planning (Hardy, 1994; St-Jean et al., 1998).

Multi-Modality Atlases. Because of the superior anatomic resolution, several digital atlases have been created using cryosection imaging. This technique allows the serial collection of photographic images from a cryoplaned specimen blockface (Bohm et al., 1983; Greitz et al., 1991; Toga et al., 1994). Using 1024^2, 24-bits/pixel digital color cameras, cryosection imaging offers a spatial resolution as high as 100 microns/voxel for whole human head cadaver preparations, or higher for isolated brain regions (Toga et al., 1997). Unlike paper atlases, digital cryosection volumes are amenable to a variety of resampling and repositioning schemes. Structures can therefore be rendered and visualized from any angle. In the *Visible Human Project* (Spitzer et al., 1996), two (male and female) cadavers were cryoplaned and imaged at 1.0 mm intervals (0.33 mm for the female data), and the entire bodies were also reconstructed via 5,000 *post mortem* CT and MRI images. The resulting digital datasets consist of over 15 gigabytes of image data. While not an atlas *per se*, the *Visible Human* data has served as the foundation for developing related atlases of regions of the cerebral cortex (Drury and Van Essen, 1997), and high-quality brain models and visualizations (Schiemann et al., 1996; Stewart et al., 1996). Using multi-modality data from a patient with a localized pathology, and more recently the *Visible Human* data, Höhne and co-workers developed a commercially available brain atlas designed for teaching neuroanatomy (VOXEL-MAN; Höhne et al., 1990, 1992; Tiede et al., 1993; Pommert et al., 1994).

Post Mortem Data Fusion. Fusion of metabolic and functional images acquired *in vivo* with *post mortem* biochemical maps provides a unique view of the relationship between brain function and pathology. Mega et al. (1997) scanned Alzheimer's patients in the terminal stages of their disease using both MRI and PET. Using elastic registration techniques (Thompson et al., 1996), these data were combined with *post mortem* histologic images showing the gross anatomy (Toga et al., 1994), a Gallyas stain of neurofibrillary tangles, and a variety of spatially indexed biochemical assays (Fig. 2). The resulting multimodality maps of the Alzheimer's disease brain relate the anatomic and histopathologic underpinnings of the disease in a standardized coordinate space. These data are further correlated with *in vivo* metabolic and perfusion maps of this disease. The resulting maps are key components of a growing disease-specific atlas (Mega et al., *this volume*).

III. Analyzing Brain Data

One of the driving forces that made anatomical templates important in brain imaging was the need to perform brain to brain comparisons. Anatomic variations severely hamper the integration and comparison of data across

subjects, and can lead to misleading results (Meltzer and Frost, 1994; Woods, 1996). Motivated by the need to standardize and pool data across subjects, and compare results across laboratories, several registration methods have been developed to align brain mapping data with an atlas. The simplest registration techniques are linear, removing global differences in brain size. Non-linear approaches, however, can eliminate even the most local size and shape differences that distinguish one brain from another. Transforming individual datasets into the shape of a single reference anatomy, or onto a 3D digital brain atlas, allows subsequent comparison of brain function across individuals (Christensen *et al.*, 1993; Ashburner et al., 1997). Interestingly, the transformations required to remove individual differences in anatomy are themselves a rich source of morphometric data (Thompson and Toga, 1999). As we shall see later (Section 10), this data can be used to create disease-specific atlases.

Spatial Normalization. In the earliest brain atlases, spatial normalization systems were proposed to transform new data to match the space occupied by the atlas. In the Talairach stereotaxic system (Talairach and Tournoux, 1988), piecewise affine transformations are applied to 12 rectangular regions of brain, to re-position the subject's brain in a defined space. The Talairach stereotaxic system rapidly became an international reporting standard for functional activation sites in PET and fMRI studies (Fox et al., 1985, 1988; Friston et al., 1989, 1991).

Use of Digital Templates. While stereotaxic methods provide a common coordinate system to pool activation data for multi-subject comparisons, the accuracy and utility of the underlying atlas is equally dependent on the anatomical template itself (Roland and Zilles, 1994). Clearly the success of any brain atlas depends on how well the anatomies of individual subjects match the representation of anatomy in the atlas. The Talairach templates, for example, are based on *post mortem* brain sections from a 60 year-old female subject. They therefore poorly reflect the *in vivo* anatomy of subjects in activation studies, and are even less representative of brains undergoing degenerative or developmental change. To address some of these limitations, a composite MRI dataset was constructed from several hundred young normal subjects (239 males, 66 females; age: 23.4±4.1 years; Evans et al., 1992, 1994). These subjects' scans were individually mapped into the Talairach system by linear transformation, intensity normalized, and averaged on a voxel-by-voxel basis. Although the resulting average brain has regions where individual structures are blurred out due to spatial variability in the population (Evans et al., 1992; 1994; see Section 10), the effect of anatomical variability in different brain areas is illustrated qualitatively by this image template. The average intensity template is part of the widely used *Statistical Parametric Mapping* package (SPM; Friston et al., 1995). Automated methods were subsequently developed to map new MRI and PET data into a common space. Because the composite MR target atlas was digital, algorithms could align new MR data with the template by maximizing a measure of intensity similarity, such as 3D cross-correlation (Collins et al., 1994,1995), ratio image uniformity (Woods et al., 1992), or mutual information (Viola et al., 1995; Wells et al., 1997). Any alignment transformation defined for one modality, such as MRI, can be identically applied to another modality, such as PET, if a previous cross-modality intrasubject registration has been performed (Woods et al., 1993). For the first time then, PET data could be mapped into stereotaxic space via a correlated MR dataset (Woods et al., 1993; Evans et al., 1994). Registration algorithms therefore made it feasible to automatically map data from a variety of modalities into an atlas coordinate space based directly on the Talairach reference system.

IV. Individualized Brain Atlases

Anatomic Variations. No two brains are the same, which presents a challenge in creating standardized atlases. Even without pathology, brain structures vary between individuals in every metric; shape, size, position and orientation relative to each other (Steinmetz et al., 1989, 1990). Due to the obvious limitations of a fixed atlas, new algorithms were developed to elastically re-shape an atlas to the anatomy of new individuals. The resulting *deformable brain atlases* more accurately project atlas data into new scans. Their uses include surgical planning (Warfield et al., 1998; St-Jean et al., 1998), anatomical labeling (Iosifescu et al., 1997) and shape measurement

(Thompson et al., 1997; Haller et al., 1997; Csernansky et al., 1998; Subsol et al., 1998). The shape of the digital atlas is adapted using local warping transformations (dilations, contractions and shearing), producing an *individualized* brain atlas (Evans et al., 1991; Miller et al., 1993; Christensen et al., 1993; Sandor and Leahy, 1994; 1995; Rizzo et al., 1995). Pioneered by Bajcsy and colleagues at the University of Pennsylvania (Broit, 1981; Bajcsy and Kovacic, 1989; Gee et al., 1993, 1995, 1998), this approach was adopted by the *Karolinska Brain Atlas* Program (Seitz et al., 1990; Thurfjell et al., 1993; Ingvar et al., 1994). Warping algorithms can transfer maps of cytoarchitecture, biochemistry, functional and vascular territories into the coordinate system of different subjects (see Toga, 1998, for a review). Intricate patterns of structural variation in anatomy can be accommodated. These transformations must allow any segment of the atlas anatomy, however small, to grow, shrink, twist and even rotate, to produce a transformation that encodes local differences in topography from one individual to another.

Non-linear mapping of raster volumes or 3D geometric atlases onto individual datasets has empowered many studies of disease. These include brain structure labeling for hippocampal morphometry in dementia (Haller et al., 1997), analysis of subcortical structure volumes in schizophrenia (Iosifescu et al., 1997; Csernansky et al., 1998), estimation of structural variation in normal and diseased populations (Collins et al., 1994; Thompson et al., 1997), and segmentation and classification of multiple sclerosis lesions (Warfield et al., 1995). Digital anatomic models can also be projected into PET data to define regions of interest for quantitative calculations of regional cerebral blood flow (Ingvar et al., 1994; Dinov et al., 1999). These template-driven segmentations require extensive validation relative to more labor-intensive manual delineation of structures, but show considerable promise in studies of disease.

Analyzing Brain Data with an Atlas. The ability to relate atlas data to a new subject's brain images also operates in reverse. By inverting the deformation field that reconfigures an atlas to match an individual, an individual's data can be nonlinearly registered with the atlas, removing subject-specific anatomical differences. Functional data then be compared and integrated across subjects, with confounding anatomical effects factored out. Since they transfer multi-subject data more accurately into a stereotaxic framework, non-linear registration algorithms are now increasingly used in functional image analysis packages (Seitz et al., 1990; Friston et al., 1995; Ashburner et al., 1997).

Because variations in structure and function are so great, and both are altered in disease, non-linear registration approaches become relevant in creating disease-specific templates. These algorithms eliminate the anatomic component of functional variation, and are required to separate variations in structure and function. They are also vital in creating deformable atlases, which offer a means to represent, and measure, variations in structure.

Intensity/Model-Driven Algorithms. Elastic registration, or *warping*, algorithms the drive a deformable atlas can be classified into two basic types (see Thompson and Toga, 1998, for a review). We briefly review these, because of their fundamental role in transferring data between scans and atlas templates, in either direction.

1. *Intensity-Driven Approaches.* These algorithms measure the similarity between the deforming atlas and the patient's scan. They then optimize the measure by tuning parameters of the deformation field. The widely-used *Automated Image Registration* (Woods et al., 1998) and *Statistical Parametric Mapping* algorithms (Ashburner et al., 1997) are examples of this approach. As the cost function is optimized, increasingly complex warping fields are expressed in terms of a 3D cosine basis (SPM) or by tuning parameters of 3D polynomials (AIR). Since they use purely mathematical criteria, intensity-driven approaches by-pass information on the topological organization of the brain. Accurate anatomic correspondences, especially at the cortex, are sometimes difficult to establish. Nonetheless, their speed and automation makes them ideal for many applications.

2. *Model-Driven Approaches.* These algorithms establish biologically constrained object-to-object correspondences in the brain. They first build large systems of anatomical models in the atlas and patient's scan (Thompson et al., 1996). This topological model of the brain's anatomy is used to derive a transformation matching anatomical surface boundaries and cortical features exactly, guiding the volumetric mapping of the atlas onto the patient (Fig. 3).

When extended to accommodate more subjects, deformations that match an atlas with each patient in a population can be used to create statistical maps of anatomy, revealing patterns of variability, asymmetry or abnormality in a group (Thompson et al., 1996, 1997). With a model-driven approach, graphical surface models represent each major anatomic system, so a comprehensive geometric atlas can be built. Average representations can be created for each anatomical element, along with statistical maps that can be visualized directly or used to guide subsequent image analysis.

Continuum-Mechanical Atlases. Many brain atlases have been developed to deform according to the principles of continuum mechanics (Broit, 1981; Bajcsy and Kovacic, 1989; Christensen et al., 1993, 1996; Davatzikos, 1996; Thompson and Toga, 1998; Gee et al., 1998). This feature is relevant to understanding how variations in structure can be encoded. In modeling the atlas deformations, differential equations are used to make the deforming atlas conform to the behavior of elastic or fluid materials. An advantage of this approach is that the well-understood mathematics enforces several desirable characteristics in the mappings. For instance, atlas-to-patient mappings should be one-to-one (i.e., the deformed atlas should not tear or self-intersect). This is surprisingly difficult to guarantee, unless continuum-mechanical or variational methods are applied (Christensen et al., 1995; Dupuis et al., 1998; *see Footnote 1*). The continuum-mechanical operators that govern the atlas deformations also have a spectral (or eigenfunction) representation that helps calculate the mappings rapidly (Miller et al., 1993; Ashburner et al., 1997).

Footnote 1. Applying Large Deformations to Brain Atlases. Christensen et al. (1995) observed that most warping methods that are used to adapt deformable brain atlases do not maintain the topological integrity of the deforming template if large deformations are required. In 2D, for example, a specification of correspondences at point landmarks is usually extended to produce a deformation field by minimizing a specific regularizing functional such as the *thin-plate spline energy* (Bookstein, 1997):

$$J_{\textbf{thin-plate}}(\mathbf{u}) = \int_{\mathbf{R}^2} [\ (\partial_{11}\mathbf{u})^2 + 2(\partial_{12}\mathbf{u})^2 + (\partial_{22}\mathbf{u})^2\ ]\ dx_1\ dx_2$$

where $\partial_{ij}\mathbf{u} = \partial^2\mathbf{u}/\partial x_i \partial x_j$, or the *membrane spline* (Amit et al., 1991; Gee et al., 1993; Ashburner et al., 1997) or *elastic body energies* (Miller et al., 1993):

$$J_{\textbf{memb}}(\mathbf{u}) = \int [\ (\partial_1 u_1)^2 + (\partial_1 u_2)^2 + (\partial_2 u_1)^2 + (\partial_2 u_2)^2\ ]\ dx_1\ dx_2$$

$$J_{\textbf{elas}}(\mathbf{u}) = \int \sum_{i=1 \text{ to } 2} \sum_{j=1 \text{ to } 2} [\ (\lambda/2)(\partial_i u_i)(\partial_j u_j) + (\mu/4)((\partial_i u_j) + (\partial_j u_i))^2\ ]\ dx_1\ dx_2$$

Since the transformations that minimize these energies do not guarantee that the deforming template remains intact after large landmark deformations, Christensen et al. (1995) suggested a way to avoid this problem. By forcing the warping field to arise by Euler integration of a continuously differentiable velocity field: $\mathbf{v}: (\mathbf{x},t) \in \Omega x[0,1] \rightarrow \mathbf{v}(\mathbf{x},t) \in R^3$, the resulting transform:

$$\mathbf{u}(\mathbf{x},t) = \mathbf{u}(\mathbf{x},0) + \int_{s=0 \text{ to } t} \mathbf{v}(\mathbf{u}(\mathbf{x},s),s)\ ds$$

is a unique diffeomorphism. Dupuis et al. (1998) further suggested that the Dirichlet problem for image matching (Joshi et al., 1995) could be reformulated by forcing the optimal velocity field to minimize quadratic energetics on the space-time element $\Omega x[0,1] = [0,1]^4 \subset R^4$, governed by a matrix constant coefficient differential operator: $\mathbf{E(v)} = \int_{\Omega x[0,1]} \|L\mathbf{v}(\mathbf{u}(\mathbf{x},t),t)\|^2\ dx\ dt$.. For matching a system of N point landmarks with this type of flow, the optimal solution was then shown (Joshi, 1998) to be derivable from the paths of the N landmarks directly, resulting in the parameterization: $\hat{\mathbf{u}}(\mathbf{x},t) = \sum_i c_i(t) G G^{\dagger}(\mathbf{x}, \hat{\mathbf{u}}(\mathbf{x}_i,t))$. Here the coefficients $c_i(t)$ are R^3-valued functions on [0,1], and $G(\mathbf{x},\mathbf{y})$ is the matrix Green's operator corresponding to L. The resulting framework for constructing diffeomorphic (smooth one-to-one) brain maps allows arbitrarily complex atlas transformations while guaranteeing that the digital template remains intact and connected under the transformation.

Statistical Templates. The deformable template framework has also been widely tested in computer vision applications where shape variability needs to be accommodated, such as written digit identification or face recognition. This makes it easier to build a statistical theory of shape for encoding brain variation, using Gaussian fields (Thompson et al., 1996a,b, 1997a,b; Davatzikos et al., 1997; Ashburner et al., 1997; Gee et al., 1998; Dupuis et al., 1998; Thirion et al., 1998; Cao and Worsley, 1999; Le Goualher et al., 1999) or Riemannian shape manifolds (Bookstein, 1997). Probabilistic transformations can then be applied to deformable anatomic templates to create a type of probabilistic atlas that measures variability and detects pathology (Thompson et al., 1997, 1998; Joshi et al., 1998; Grenander and Miller, 1998).

Individualizing an Atlas. To understand how deformable atlases work, consider the deforming atlas to be embedded in a 3D elastic or fluid medium (Fig. 4). The medium is subjected to distributed internal forces, which reconfigure it, and lead the image to match the target. In elastic media, the displacement vector field $\mathbf{u}(\mathbf{x})$ resulting from internal driving forces $\mathbf{F}(\mathbf{x})$ (called '*body forces*') obeys the Navier-Stokes equilibrium equations for linear elasticity:

$$\mu\nabla^2\mathbf{u} + (\lambda+\mu)\nabla(\nabla^T \bullet \mathbf{u}(\mathbf{x})) + \mathbf{F}(\mathbf{x}) = \mathbf{0}, \ \forall \mathbf{x} \in R \qquad (1).$$

Here R is a discrete lattice representation of the atlas, $\nabla^T \bullet \mathbf{u}(\mathbf{x}) = \sum \partial u_j / \partial x_j$ is the cubical dilation of the medium, ∇^2 is the Laplacian operator, and Lamé's coefficients λ and μ refer to the elastic properties of the medium. Body forces, $\mathbf{F(x)}$, drive the atlas into correspondence with similar regions in the patient. In a model-based approach, these forces are computed from a large set of anatomical surface models (Thompson and Toga, 1998), so that the deformations of structure boundaries are propagated to the image volume. In an intensity-based approach, the body forces are derived from the gradient of a local cost function. The cost function is a metric designed to capture how well the atlas is aligned with the patient's scan. Common measures include squared differences in normalized pixel intensities (Christensen et al., 1993; Woods et al., 1993, 1998; Ashburner et al., 1997), ratio image uniformity (Woods et al., 1992), regional correlation (Bajcsy and Kovacic, 1989; Collins et al., 1995), or mutual information (Kim et al., 1997; Kjems et al., 1999). If an elastic model is used, the equilibrium equations are solved numerically by finite difference, finite element, or spectral methods, and the 3-dimensional deformation field $\mathbf{u}(\mathbf{x})$ warps the atlas into register with the target scan.

Massively Parallel Implementations. Recently, Christensen *et al*. (1993, 1995, 1996) proposed a viscous-fluid based warping transform, to individualize a labeled atlas and segment hippocampal anatomy in new patients' scans (*cf*. Haller et al., 1997; Csernansky et al., 1998). Manual tag points first roughly align the atlas and patient's anatomy. An intensity-based force (2) then drives a large-distance non-linear fluid evolution of the neuroanatomic template. With the introduction of concepts such as deformation velocity and a Eulerian reference frame, the energetics of the deformed medium are hypothesized to be relaxed in a highly viscous fluid:

$$\mathbf{F}((\mathbf{x},\mathbf{u}(\mathbf{x},t)) = -(T(\mathbf{x}-\mathbf{u}(\mathbf{x},t))-S(\mathbf{x}))\ \nabla T\big|_{\mathbf{x}-\mathbf{u}(\mathbf{x},t)} \qquad (2)$$

$$\mu\nabla^2\mathbf{v}(\mathbf{x},t) + (\lambda+\mu)\nabla(\nabla^T \bullet \mathbf{v}(\mathbf{x},t)) + \mathbf{F}(\mathbf{x},\mathbf{u}(\mathbf{x},t)) = \mathbf{0} \qquad (3)$$

$$\partial\mathbf{u}(\mathbf{x},t)/\partial t = \mathbf{v}(\mathbf{x},t) - \nabla\mathbf{u}(\mathbf{x},t)\mathbf{v}(\mathbf{x},t) \qquad (4)$$

The deformation velocity of the atlas (3) is governed by the creeping flow momentum equation for a Newtonian fluid, and the conventional displacement field in a Lagrangian reference system (4) is connected to an Eulerian velocity field by the relation of material differentiation. Experimental results were excellent (Christensen *et al*., 1996). Nonetheless, both elastic and fluid algorithms contain core systems of up to 0.1 billion simultaneous partial differential equations (1 or (2)-(4)). In early implementations, deformable registration of a 128^3 MRI atlas to a patient took 9.5 and 13 hours for elastic and fluid transforms, respectively, on a 128×64 DECmpp1200Sx/Model 200 MASPAR (Massively Parallel Mesh-Connected Supercomputer). This spurred work

to modify the algorithm to individualize atlases on standard single-processor workstations (Thirion, 1995; Bro-Nielsen and Gramkow, 1996; Freeborough and Fox, 1998).

Bro-Nielsen and Gramkow (1996) used the eigenfunctions of the Navier-Stokes differential operator $L = \mu\nabla^2+(\lambda+\mu)\nabla(\nabla^T\bullet)$, which governs the atlas deformations, to derive a Green's function solution $\mathbf{u^*(x)}=\mathbf{G(x)}$ to the impulse response equation $L\mathbf{u^*(x)}=\delta\mathbf{(x-x_0)}$. This speeds up the core registration step by a factor of 1000. The solution to the full PDE $L\mathbf{u(x)}=-\mathbf{F(x)}$ was approximated as a rapid filtering operation on the 3D arrays representing body force components:

$$\mathbf{u(x)} = -\int_{\Omega} \mathbf{G(x-r)}.\mathbf{F(r)}\, d\mathbf{r} = -(\mathbf{G}*\mathbf{F})\mathbf{(x)}, \qquad (5)$$

where **G*** represents convolution with the impulse response filter. As noted in (Gramkow and Bro-Nielsen, 1997), a recent fast, 'demons-based' warping algorithm (Thirion, 1995) calculates the atlas flow velocity by regularizing the force field driving the template with a Gaussian filter (*cf.* Collins et al., 1994). Since this filter may be regarded as a separable approximation to the continuum-mechanical filters derived above, interest has focused on deriving additional separable (and therefore computationally fast) filters to create subject-specific brain atlases and rapidly label new images (Gramkow, 1996; Lester et al., 1999). Fast multi-grid solvers have also accelerated systems for atlas-based segmentation and labeling (Dengler and Schmidt, 1988; Bajcsy and Kovacic (1989); Collins et al., 1994, 1995; Gee et al., 1993,1995; Schormann et al., 1996). Some of these now have sufficient speed for real-time surgical guidance applications (Warfield et al., 1998).

V. Model-Driven Deformable Atlases

The extreme difficulty of finding structures in new patients based on intensity criteria alone has led several groups to develop model-driven deformable atlases (Thompson and Toga, 1997; Toga and Thompson, 1997). Anatomic models provide an explicit geometry for individual structures in each scan, such as landmark points, curves or surfaces. Because the digital models reside in the same stereotaxic space as the atlas data, surface and volume models stored as lists of vector coordinates are amenable to digital transformation, as well as geometric and statistical measurement (Thompson et al., 1996). The underlying 3D coordinate system is central to all atlas systems, since it supports the linkage of structure models and associated image data with spatially-indexed neuroanatomic labels, preserving spatial information and adding anatomical knowledge.

In Sections 6-10, we show how anatomical models can create probabilistic atlases and disease-specific templates. Statistical averaging of models provides a means to analyze brain structure in morphometric projects, localizing disease-specific differences with statistical and visual power. We first describe how models can drive deformable atlases, measuring patient-specific differences in considerable detail.

When deforming an atlas to match a patient's anatomy, mesh-based models of anatomic systems help guide the mapping of one brain to another. Anatomically-driven algorithms guarantee biological as well as computational validity, generating meaningful object-to-object correspondences, especially at the cortex. Ultimately, accurate warping of brain data requires:

(1) matching entire systems of anatomic *surface* boundaries, both external and internal, and
(2) matching relevant curved and point landmarks, including ones within the surfaces being matched (e.g., primary sulci at the cortex, tissue type boundaries at the ventricular surface).

In our own model-driven warping algorithm (Thompson and Toga, 1996, 1997, 1998), systems of model surfaces are first extracted from each dataset, to guide the volumetric mapping. The model surfaces include many

functional, cytoarchitectonic and lobar boundaries in 3 dimensions. Both the surfaces and the landmark curves within them are reconfigured to match their counterparts in the target datasets exactly. We will discuss this approach in some detail.

Anatomical Models. Since much of the functional territory of the human cortex is buried in cortical folds or *sulci*, a generic structure is built to model them (Fig. 3,5; Thompson and Toga, 1996). The underlying data structure is a connected system of surface meshes, in which the individual meshes are parametric. These surfaces are 3D sheets that divide and join at curved junctions to form a connected network of models. With the help of these meshes, each patient's anatomy is modeled in sufficient detail to be sensitive to subtle differences in disease. Separate surfaces model the deep internal trajectories of features such as the parieto-occipital sulcus, the anterior and posterior calcarine sulcus, the Sylvian fissure, and the cingulate, marginal and supracallosal sulci in both hemispheres. Additional gyral boundaries are represented by parameterized curves lying in the cortical surface. The ventricular system is modeled as a closed system of 14 connected surface elements whose junctions reflect cytoarchitectonic boundaries of the adjacent tissue (Fig. 6; Thompson and Toga, 1998). Information on the meshes' spatial relations, including their surface topology (*closed* or *open*), anatomical names, mutual connections, directions of parameterization, and common 3D junctions and boundaries is stored in a hierarchical graph structure. This ensures the continuity of displacement vector fields defined at mesh junctions.

Surface Parameterization. After imposing an identical regular grid structure on anatomic surfaces from different subjects (Fig. 5), the explicit geometry can be exploited to drive and constrain correspondence maps that associate anatomic points in different subjects. Structures that can be extracted automatically in parametric form include the external cortical surface (discussed in Section 8), ventricular surfaces, and several deep sulcal surfaces. Recent success of sulcal extraction approaches based on deformable surfaces (Vaillant et al., 1997) led us to combine a 3D skeletonization algorithm with deformable curve and surface governing equations to automatically produce parameterized models of cingulate, parieto-occipital, and calcarine sulci, without manual initialization (Zhou et al., 1999). Additional, manually-segmented surfaces can also be given a uniform rectilinear parameterization using algorithms described in (Thompson et al., 1996a,b), and used to drive the warping algorithm. Each resultant surface mesh is analogous in form to a uniform rectangular grid, drawn on a rubber sheet, which is subsequently stretched to match all data points. Association of points on each surface with the same mesh coordinate produces a dense correspondence vector field between surface points in different subjects. This procedure is carried out under stringent conditions (*see Footnote 2*), to ensure that landmark curves and points known to the anatomist appear in corresponding locations in each parametric grid.

Footnote 2. For example, the calcarine sulcus (see Fig. 5) is partitioned into two meshes (*CALCa* and *CALCp*). This ensures that the complex 3D curve forming their junction with the parieto-occipital sulcus is accurately mapped under both the surface displacement and 3D volumetric maps reconfiguring one anatomy into the shape of another. Fig. 5(b) illustrates this procedure, in a case where 3 surface meshes in one brain are matched with their counterparts in a target brain. Section 8 describes a separate approach, which is needed to match systems of curves lying *within* a surface, such as the cortex, with their counterparts in a target brain.

Displacement Maps. For each surface mesh $\mathbf{M_l^p}$ in a pair of scans $\mathbf{A_p}$ and $\mathbf{A_q}$ we define a 3D displacement field:

$$\mathbf{W_l^{pq}}[\mathbf{r_l^p}(u,v)] = \mathbf{r_l^q}(u,v)-\mathbf{r_l^p}(u,v) \qquad (6)$$

carrying each surface point $\mathbf{r_l^p}(u,v)$ in $\mathbf{A_p}$ into structural correspondence with $\mathbf{r_l^q}(u,v)$, the point in the target mesh parameterized by rectangular coordinates (u,v). This family of high-resolution transformations, applied to individual meshes in a connected system deep inside the brain, elastically transforms elements of the surface system in one 3D image to their counterparts in the target scan. Weighted linear combinations of radial functions, describing the influence of deforming surfaces on points in their vicinity, extend the surface-based deformation to

the whole brain volume (see Fig. 7). Recent extensions of the core algorithm to include continuum-mechanical, and other filter-based models of deformation (Thompson and Toga, 1998; *cf.* Joshi et al., 1995; Davatzikos, 1996; Schiemann and Höhne, 1997; Gabrani and Tretiak, 1999) have yielded similar encouraging results. Fig. 7 shows how the algorithm performs on cryosection data.

VI. Probabilistic Atlases

Encoding Anatomic Variability. Many morphometric studies focus on identifying systematic alterations in anatomy in a variety of diseases (Table 1). These studies are complicated by the substantial overlap between measures of normal and diseased anatomy. Normal anatomic complexity makes group specific patterns hard to discern. However, disease-specific variants may be easier to localize by creating average models of anatomy, rather than deriving volumetric descriptors.

In response to these challenges, *probabilistic atlases* are research tools that retain information on anatomic and functional variability (Mazziotta *et al*., 1995; Thompson et al., 1997). A probabilistic atlas solves many of the limitations of a fixed atlas in representing highly variable anatomy. As the subject database increases in size and content, the digital form of the atlas allows efficient statistical comparisons of individuals or groups. In addition, the population that an atlas represents can be stratified into subpopulations to represent specific disease types, and subsequently by age, gender, handedness, or genetic factors.

Parametric Mesh Modeling. Parametric meshes (Thompson et al., 1996a,b) offer a means to create average models of anatomy. Once anatomical data is transformed to a standardized coordinate space, such as the Talairach space, a computational grid structure can be imposed on anatomical surface boundaries. These mesh models represent boundary point locations in stereotaxic coordinates (Fig. 5). Averaging of corresponding grid points across subjects results in an average surface model for each structure. At the same time, knowledge of each subject's deviations from the group average anatomy can be retained as a vector displacement map (Fig. 5). After storing these maps from large numbers of subjects, local biases in the magnitude and direction of anatomic variability can be displayed as a map. Variability maps for deep sulcal surfaces are shown in Fig. 8. In these maps, the color shows the root mean square magnitude of the displacement vectors that map individuals to the group mean. Separate maps are displayed for elderly normals (mean age: 72.9 ± 5.6 yrs.; all 10 right-handed), and demographically matched Alzheimer's patients (age: 71.9 ±10.7 yrs.; all 10 right-handed; mean Mini-Mental State Exam score: 19.7 ± 5.7, out of 30). As expected, there is an extraordinary increase in anatomical variability from deep structures (0-5 mm at the corpus callosum) to peak r.m.s. values of 12-13 mm at the posterior Sylvian fissures (Thompson et al., 1998). In AD however, Sylvian fissure variability rose extremely sharply from an SD of 6.0 mm rostrally on the left to 19.6 mm caudally. Underlying atrophy and possible left greater than right degeneration of perisylvian gyri (Loewenstein *et al.*, 1989; Siegel *et al*., 1996) may widen the Sylvian fissure, superimposing additional individual variation and asymmetry on that seen in normal aging.

Brain Asymmetry. A third feature observable from the average anatomical models (Fig. 8) is that consistent patterns of brain asymmetry can be mapped, despite wide variations in asymmetry in individual subjects. In dementia, the increased cortical asymmetry probably reflects asymmetric progression of the disease. Fig. 9 shows average maps of the lateral ventricles, again from Alzheimer's Disease and matched elderly normal populations. As expected, the ventricles are significantly enlarged in dementia. Notice, however, that a pronounced asymmetry is observed in both groups (left volume larger than right, $p < 0.05$). This is an example of an effect that becomes clear after group averaging of anatomy, and is not universally apparent in individual subjects. It is, however, consistent with prior volumetric measurements (Shenton et al., 1991; Aso et al., 1995). Anatomical averaging can also be cross-validated with a traditional volumetric approach. Occipital horns were on average 17.1% larger on the left in the normal group (4070.1 ± 479.9 mm^3) than on the right (3475.3 ± 334.0 mm^3; $p < 0.05$), but no

significant asymmetry was found for the superior horns (*left:* 8658.0 ± 976.7 mm^3; *right:* 8086.4 ± 1068.2 mm^3; $p > 0.19$) or for the inferior horns (*left:* 620.6 ± 102.6 mm^3; *right:* 573.7 ± 85.2 mm^3; $p > 0.37$). The asymmetry is clearly localized in the 3D group average anatomic representations. In particular, the occipital horn extends (on average) 5.1 mm more posteriorly on the left than the right. The capacity to resolve asymmetries in a group atlas can assist in studies of disease-specific cortical organization (Thompson et al., 1997; Mega et al., 1998; Zoumalan et al., 1999; Narr et al., 1998, 1999).

Corpus Callosum Differences. We also tested the ability of anatomical averaging to identify disease-specific patterns in clinical populations. First, the approach was used to detect pre-clinical hippocampal atrophy in patients with minimal cognitive impairment (Kwong et al., 1999; Mega et al., *this volume*). To identify more focal effects, we attempted to identify regionally selective patterns of callosal change in patient groups with Alzheimer's disease and schizophrenia (Thompson et al., 1998; Narr et al., 1999). The mid-sagittal callosum was first partitioned into 5 sectors (Fig. 10; Duara *et al.* (1991); Larsen *et al*., 1992). This roughly segregates callosal fibers from distinct cortical regions. In AD, focal fiber loss was expected at the callosal isthmus (sector 2) whose fibers selectively innervate the temporo-parietal regions with early neuronal loss and perfusion deficits (Brun and Englund, 1981). Consistent with this hypothesis, a significant area reduction at the isthmus was found, reflecting a dramatic 24.5% decrease from 98.0 ± 8.6 mm^2 in controls to 74.0 ± 5.3 mm^2 in AD ($p < 0.025$). Terminal sectors (1 and 5) were not significantly atrophied, and the central midbody sector showed only a trend toward significance (16.6% mean area loss; $p < 0.1$), due to substantial inter-group overlap. Average boundary representations, however, localized these findings directly. At the isthmus, average models in AD showed a pronounced shape inflection at stereotaxic location (0.0,-25.0,19.0) (see Fig. 10).

Gender in Schizophrenia. Different shape alterations were observed in schizophrenia (Narr et al., 1999; Fig. 11). A significant bowing effect was observed, reflecting enlargement of the underlying 3rd ventricle. By creating separate average models for male and female patients, significant gender effects also emerged (Fig. 11(a)-(d)). The greater bowing effect in male than female patients was confirmed by multivariate analysis of variance, and is highlighted in the average anatomic templates. As emphasized by this example, even if no sex difference is present in normal callosal morphology (see Thompson et al., 1999, for a review of this controversy), this does not preclude sex effects from interacting with morphometric abnormalities in diseased populations. In schizophrenia, there is typically a later age of onset in female schizophrenics, and hereditary factors may be unevenly distributed between the sexes (De Lisi et al., 1989; Waddington, 1993; Colombo et al., 1993). Stratification of probabilistic atlases by gender and other genetic factors provides a computationally fast way to visualize these effects and relate them to epidemiologic data (Mazziotta et al., 1995; Mega et al., 1998; Zoumalan et al., 1999; Blanton et al., 1999; Le Goualher et al., 1999).

VII. Atlas-Based Pathology Detection

Deformable Probabilistic Atlases. As noted earlier, *warping* algorithms create deformation maps (Fig. 7) that indicate 3D patterns of anatomic differences between any pair of subjects. By defining probability distributions on the space of deformation transformations which drive the anatomy of different subjects into correspondence (Grenander, 1976; Amit et al., 1991; Grenander and Miller, 1994; Thompson and Toga, 1997; Thompson et al., 1997), statistical parameters of these distributions can be estimated from databased anatomic data to determine the magnitude and directional biases of anatomic variation. Encoding of local variation can then be used to assess the severity of structural variants outside of the normal range, which, in brain data, may be a sign of disease (Thompson et al., 1997).

Encoding Brain Variation. To see if disease-specific features could be detected in individual patients, we developed a *random vector field* approach to construct a population-based brain atlas (Thompson and Toga,

1997). Briefly, given a 3D MR image of a new subject, a warping algorithm calculates a set of high-dimensional volumetric maps, elastically matching this image with other scans from an anatomic image database. Target scans are selected from subjects matched for age, handedness, gender, and other demographic factors (Thompson et al., 1997, 1998). The resulting family of volumetric warps provides empirical information on local variability patterns. A probability space of random transformations, based on the theory of anisotropic Gaussian random fields (Thompson et al., 1997), is then used to encode the variations. For the cortex, specialized approaches are needed to represent variations in gyral patterns (Thompson et al., 1997; Thompson and Toga, 1998; Section 8). Confidence limits in stereotaxic space are determined, for points in the new subject's brain, enabling the creation of color-coded probability maps to highlight and quantify regional patterns of deformity (Fig. 12).

Comparing a Subject with an Atlas. In one validation experiment (Thompson et al., 1997; Fig. 12), probability maps were created to highlight abnormal deviations in the callosal and midline anatomy of a tumor patient. The two regions of metastatic tissue induced marked distortions in the normal architecture of the brain. After storing variations in deep surface anatomy as a spatially-adaptive covariance tensor field (Thompson et al., 1997), probability maps were generated for the tumor patient. In the tumor patient, the herniation effects apparent in the blockface imagery (Fig. 12(a)) were detected in the probability maps of structures near the lesion sites (Fig. 12(b)).

In this approach, the tensor field stores information on the preferred directions of normal variability. For example, it retains information that lateral displacements of the callosum are more unlikely than vertical displacements in a normal group. Local computation of the variance components also means that confidence limits for abnormal structure are appropriately relaxed in regions of high anatomic variability, so normal differences are not signaled as deficits.

Anisotropic Gaussian Fields. In a probabilistic atlas, well-defined statistical criteria are required to identify significant differences in brain structure. These criteria can be formulated in different ways, depending on the attribute whose statistical variation is being modeled. One approach is to use the theory of Gaussian random fields, a modeling technique used widely in functional image analysis (e.g., SPM; Friston et al., 1995). By contrast with functional signals, which are generally treated as random *scalar* fields, the deformation maps that quantify structural differences are treated as random *vector* fields. Instead of a field of variance values, the variability of the deformation vectors, and their directional tendencies, are stored using a covariance tensor at each anatomical point (Thompson et al., 1996; Cao and Worsley, 1999).

In one study (Thompson et al., 1997; *cf.* Cao and Worsley, 1999), we developed an approach to detect brain structure differences between two groups, or between an individual subject and a database of demographically matched subjects. Suppose $\mathbf{W}_{ij}(\mathbf{x})$ is the deformation vector required to match the structure at position $\mathbf{x}$ in an atlas template with its counterpart in subject *i* of group *j*. (If surface models are being analyzed, rather than full brain volumes (Thompson and Toga, 1998), $\mathbf{W}_{ij}(\mathbf{x})$ is the deformation vector matching parametric mesh node $\mathbf{x}(u,v)$ with its counterpart in subject *i* of group *j*.) We then model the deformations as:

$$\mathbf{W}_{ij}(\mathbf{x}) = \boldsymbol{\mu}_j(\mathbf{x}) + \boldsymbol{\Sigma}(\mathbf{x})^{1/2}\boldsymbol{\varepsilon}_{ij}(\mathbf{x}). \qquad (7)$$

Here $\boldsymbol{\mu}_j(\mathbf{x})$ is the mean deformation for group *j*, and $\boldsymbol{\Sigma}(\mathbf{x})$ is a non-stationary, anisotropic covariance tensor field (Section 9), which relaxes the confidence threshold for detecting abnormal structure in regions where normal variability is extreme, $\boldsymbol{\Sigma}(\mathbf{x})^{1/2}$ is the upper triangular Cholesky factor tensor field, and $\boldsymbol{\varepsilon}_{ij}(\mathbf{x})$ is a trivariate random vector field whose components are independent stationary Gaussian random fields.

Deformation-Based Morphometry. A T^2 or F statistic that indicates evidence of significant difference in

deformations between the groups is calculated at each lattice location in a 3D image or parameterized 3D surface, to form a statistic image (Thompson et al., 1997). Specialized algorithms, using corrections for the metric tensor of the underlying surface, are required to calculate these fields at the cortex (*see next Section*). Under the null hypothesis of no abnormal deformations, the statistic image is approximated by a T^2 random field. Specifically, the significance of a difference in brain structure between two subject groups (*e.g.*, patients and controls) of N_1 and N_2 subjects is assessed by calculating the sample mean and variance of the deformation fields (j=1,2):

$$\mathbf{W}^{\mu}{}_j(\mathbf{x}) = \sum_{i=1 \text{ to } Nj} \mathbf{W}_{ij}(\mathbf{x}) \,/\, N_j$$

$$\mathbf{\Psi}(\mathbf{x})=(1 \,/\, N_1+N_2-2)\{ \sum_{j=1 \text{ to } 2} \sum_{i=1 \text{ to } Nj} [\mathbf{W}_{ij}(\mathbf{x})- \mathbf{W}^{\mu}{}_j(\mathbf{x})][\mathbf{W}_{ij}(\mathbf{x})- \mathbf{W}^{\mu}{}_j(\mathbf{x})]^{\mathbf{T}}\}.$$

and computing the following statistical map (Thompson et al, 1997; Cao and Worsley, 1999):

$$T^2(\mathbf{x})= \{N_1N_2 \,/\, (N_1+N_2)\,(N_1+N_2-2)\}\, [\, \mathbf{W}^{\mu}{}_2(\mathbf{x}) - \mathbf{W}^{\mu}{}_1(\mathbf{x})]^{\mathbf{T}}\, [\mathbf{\Psi}(\mathbf{x})]^{-1} [\, \mathbf{W}^{\mu}{}_2(\mathbf{x}) - \mathbf{W}^{\mu}{}_1(\mathbf{x})],$$

Under the null hypothesis, $(N_1+N_2-2)T^2(\mathbf{x})$ is a stationary Hotelling's T^2-distributed random field. At each point, if we let $\nu=(N_1+N_2-2)$ and we let the dimension of the search space be d=3, then:

$$F(\mathbf{x})=((\nu-d+1)/d)T^2(\mathbf{x}) \sim F_{\,d,(\nu-d+1)}.$$

In other words, the field can be transformed point-wise to a Fisher-Snedecor F distribution (Thompson et al., 1997). To obtain a p-value for the effect that is adjusted for the multiple comparisons involved in assessing a whole field of statistics, Cao and Worsley (1999) examined the distribution of the global maximum T^2_{max} of the resulting T^2-distributed random field under the null hypothesis. The resulting probability that $T^2(\mathbf{x})$ ever exceeds a fixed high threshold T^2_{max} is approximated by the expected Euler characteristic $E[\chi(A(T^2_{max}))]$ of the excursion sets of the Hotelling's T^2-distributed random field above the threshold T^2_{max}. Then $p[T^2_{max} \geq t]$ is approximated by $\sum_{n=0 \text{ to } d} R_n\rho_n(t)$, where the number of n-dimensional resolution elements $R_n=V_n/(FWHM)^n$ depends on the effective full-width-at-half-max (FWHM) of the component Gaussian images $\boldsymbol{\varepsilon}_{ij}(\mathbf{x})$, and on the Euler characteristic (V_0), caliper diameter ($V_1/2$), surface area ($2V_2$) and volume (V_3) of the search region. The n-dimensional EC densities are given by (Cao and Worsley, 1999):

$\rho_0(t) = \int_{t \text{ to } \infty}[\Gamma((\nu+1)/2)/\,(\nu\pi)^{1/2}\Gamma(\nu/2)].[1+(u^2/\nu)]^{-1/2(\nu+1)}\, du,$
$\rho_1(t) = ((4 \ln 2)^{1/2}/2\pi).[1+(t^2/\nu)]^{-1/2(\nu-1)},$
$\rho_2(t) = ((4 \ln 2)/(2\pi)^{3/2}).[\Gamma((\nu+1)/2)/\,(\nu/2)^{1/2}\Gamma(\nu/2)].[t[1+(t^2/\nu)]^{-1/2(\nu-1)}],$
$\rho_3(t) = ((4 \ln 2)^{3/2}/(2\pi)^2).[((\nu-1)/\nu)t^2-1].[1+(t^2/\nu)]^{-1/2(\nu-1)}.$

The global maximum of the random deformation field, or derived tensor fields (Thompson et al., 1998), can be used to test the hypothesis of no structural change in disease (Worsley, 1994a,b; Cao and Worsley, 1999). Similar multivariate linear models can be used to test for the effect of explanatory variables (e.g., age, gender, clinical test scores) on a set of deformation field images (Ashburner et al., 1998; Gaser et al., 1998). This can help explore linkages between atlas descriptions of variance and behavioral or cognitive parameters (Mega et al., 1998; Fuh et al., 1998; Zoumalan et al., 1999)

Pattern-Theoretic Approaches. In a related approach based on pattern theory (Grenander and Miller, 1998), a spectral approach to representing anatomic variation is developed. Deformation maps expressing variations in normal anatomies are calculated, with a non-linear registration procedure based on continuum mechanics (Miller et al., 1993; Christensen et al., 1993). Each deformation map is expanded in terms of the

eigenfunctions of the governing operator that controls the transformations (such as the Laplacian ∇^2 (Ashburner et al., 1997) or Cauchy-Navier operator $(\lambda+\mu)\nabla(\nabla\bullet) + \mu\nabla^2$ (Christensen et al., 1996). Gaussian probability measures are defined on the resulting sequences of expansion coefficients (Amit et al., 1991; Grenander and Miller, 1998). Essentially this spectral formulation is a model of anatomic variability. Once the model parameters σ_k are learned (see *Footnote 3*), every subject's anatomy can be represented by a feature vector $(z_1,\ldots,z_n)$, whose elements are just the coefficients of the deformation field required to match their particular anatomy with a mean anatomical template. If the parameters of anatomical variation are altered in disease, a pattern classifier can classify new subjects according to their statistical distance from the diseased group mean relative to the normal group mean (Thompson et al., 1997; Joshi et al., 1998). From a validation standpoint, the operating characteristics of such a system can be investigated (i.e., false positives versus false negatives; Thompson et al., 1997; Joshi et al., 1998). Currently being tested as a framework to encode anatomic variation, these deformable atlas systems show considerable promise in identifying disease-specific differences (Haller et al., 1997; Joshi et al., 1998).

Footnote 3. In Grenander's formalism, the distribution of the random deformation fields **u(x)** is assumed to satisfy the stochastic differential equation:

$$L(\mathbf{u}(\mathbf{x})) = \mathbf{e}(\mathbf{x}). \qquad (8)$$

Here L is the operator governing the deformation and $\mathbf{e}(\mathbf{x})$ is a 3×1 random noise vector field, whose coefficients in L's eigenbasis are zero-mean independent Gaussian variables with variances $\sigma_k^{\,2}$. If the differential operator L has eigenbasis $\{\varphi_k\}$ with eigenvalues $\{\lambda_k\}$, a probability density can be defined directly on the deformation field's expansion coefficients $(z_1,\ldots,z_n)$. If

$$\mathbf{u}(\mathbf{x}) = \Sigma_k z_k \varphi_k(\mathbf{x}) \qquad (9)$$

then:

$$p(z_1,\ldots,z_n) = \exp -(1/2)(\Sigma_{k=1 \text{ to } n}\, log\{2\pi\sigma_k^{\,2}/\lambda_k^{\,2}\} + \Sigma_{k=1 \text{ to } n}\, \{|\lambda_k z_k|^2/\sigma_k^{\,2}\}) \qquad (10)$$

Bayesian Pattern Recognition. Pattern recognition algorithms for automated identification of brain structures can benefit greatly from encoded information on anatomic variability (Ashburner et al., 1998; Gee et al., 1998; Vaillant and Davatzikos, 1999). We recently developed a Bayesian approach to identify the *corpus callosum* in each image in an MRI database (Pitiot et al., 1999). The shape of a deformable curve (Fig. 13, *panel 7*) is progressively tuned to optimize a mathematical criterion measuring how likely it is that it has found the corpus callosum. The measure includes terms that reward contours based on their agreement with a diffused edge map (*panels 7-9*), their geometric regularity, and their statistical abnormality when compared with a distribution of normal shapes. As we have seen, by averaging contours derived manually from an image database, structural abnormalities associated with Alzheimer's Disease and schizophrenia were identified (Fig. 10,11; Thompson et al., 1998; Narr et al., 1999). Automated parameterization of structures will accelerate the identification and analysis of disease-specific structural patterns.

VIII. Cortical Modeling

Cortical morphology is notoriously complex, and presents unique challenges in anatomic modeling. The cortex is also severely affected in disorders such as Alzheimer's disease, Pick's disease and other dementias, by tumor growth, and in cases of epilepsy, cortical dysplasias, and schizophrenia.

A major challenge in investigations of disease is to determine (1) whether cortical organization is altered, and if so, which cortical systems are implicated, and (2) whether normal features of cortical organization are lost, such as sulcal pattern asymmetries. This requires methods to create (1) a well-resolved average model of the cortex

specific for a diseased group, and (2) a statistical framework to compare these average models with normative data.

Averaging Images or Averaging Geometry. In an atlasing context, it would be ideal to create a disease-specific template for a clinical group with well-resolved anatomical features in their mean anatomical configuration. Unfortunately this cannot be achieved by averaging together structural images in the traditional way, after a simple linear transformation to a standard space (Evans et al., 1994). If images are averaged in this way, cortical patterns are washed away due to wide variations in gyral organization. We describe a way to avoid this. First, an average cortical surface model is created with well-resolved gyral features in the group mean configuration. Continuum-mechanical mappings are then used to bring each subject's gyral pattern into correspondence with the average cortex. Maps of cortical variation are created as a by-product. Finally, a high-dimensional mapping (driven by 84 structures per brain) elastically deforms each brain into the group mean geometric configuration. Once elastically reconfigured, the scan intensities are averaged on a voxel-by-voxel basis to produce a group-specific atlas template with a well-resolved cortex. Disease-specific templates in Alzheimer's Disease and schizophrenia will be used to illustrate this method.

Cortical Matching. Cortical anatomy can be compared, between a pair of subjects, by computing the warped mapping that elastically transforms one cortex into the shape of the other. These transformations can also match large networks of gyral and sulcal features with their counterparts in the target brain (Thompson and Toga, 1996, 1997; Davatzikos, 1996; Van Essen et al., 1997; Fischl et al., 1999). Differences in cortical organization prevent exact gyrus-by-gyrus matching of one cortex with another. Nonetheless, an important intermediate goal has been to match a comprehensive network of sulcal and gyral elements that are consistent in their incidence and topology across subjects (Ono et al., 1990; Leonard et al., 1996; Kennedy et al., 1998; *see Footnote 4*).

Footnote 4. Our method (Thompson and Toga, 1996) is conceptually similar to those of Dale and Sereno (1993), Davatzikos (1996) and Fischl et al. (1999). 3D active surfaces (Cohen and Cohen, 1992) extract parametric representations of each subject's cortex, by deforming a tiled spherical mesh into the shape of the cortex. On these surface models, corresponding networks of anatomical curves are identified. Specifically, 36 parametric curves are created per subject to represent the major elements of the gyral pattern. These include the superior and inferior frontal, central, postcentral, intraparietal, superior and inferior temporal, collateral, olfactory and occipito-temporal sulci, as well as the Sylvian fissures. Additional 3D curves are drawn in each hemisphere to represent gyral limits at the interhemispheric margin (Thompson et al., 1997). Stereotaxic locations of contour points derived from the data volume are then redigitized to produce 36 uniformly parameterized cortical contours per brain, representing the primary gyral pattern of each subject (Thompson et al., 1997). The transformation relating these networks is expressed as a vector flow field in the parameter space of the cortex (Fig. 14). This vector flow field in parameter space indirectly specifies a correspondence field in 3D, which drives one cortical surface into the shape of another. This mapping not only matches overall cortical geometry, but matches the entire network of the 36 landmark curves with their counterparts in the target brain, and thus is a valid encoding of cortical variation.

Spherical, Planar Maps of Cortex. Several simpler maps of the cortex are made to help calculate the transformation. Because each subject's cortical model is arrived at by deforming a spherical mesh (MacDonald et al., 1993; Thompson and Toga, 1996; Davatzikos et al., 1996), any point on the cortex maps to exactly one point on the sphere, and a *spherical map* of the cortex is made which indexes sulcal landmarks in the normally folded brain surface. These spherical locations, indexed by two parameters, can also be mapped to a plane (Fig. 14; Thompson et al., 1997; Thompson and Toga, 1998). A flow field is then calculated that elastically warps one flat map onto the other (Fig. 15; or equivalently, one spherical map to the other). On the sphere, the parameter shift function $\mathbf{u(r)}:\Omega \rightarrow \Omega$, is given by the solution $F_{pq}:\mathbf{r}\rightarrow\mathbf{r}-\mathbf{u}(\mathbf{r})$ to a curve-driven warp in the spherical parametric space $\Omega=[0,2\pi)\times[0,\pi)$ of the cortex (Thompson et al., 1996, 1998). For points $\mathbf{r}=(r,s)$ in the parameter space, a system of simultaneous partial differential equations can be written for the flow field $\mathbf{u}(\mathbf{r})$:

$$L^{\ddagger}(\mathbf{u(r)}) + \mathbf{F}(\mathbf{r}-\mathbf{u(r)}) = \mathbf{0},\ \forall \mathbf{r}\in\Omega,$$
$$\mathbf{u}(\mathbf{r}) = \mathbf{u_0}(\mathbf{r})\ ,\ \forall \mathbf{r}\in M_0\cup M_1. \qquad (8)$$

Here M_0, M_1 are sets of points and (sulcal or gyral) curves where displacement vectors $\mathbf{u}(\mathbf{r}) = \mathbf{u_0}(\mathbf{r})$ matching corresponding anatomy across subjects are known. The flow behavior is modeled using equations derived from continuum mechanics, and these equations are governed by the Cauchy-Navier differential operator $L = \mu\nabla^2+(\lambda+\mu)\nabla(\nabla^T\bullet)$ with body force $\mathbf{F}$ (Thompson et al., 1996, 1998; Grenander

and Miller, 1998). The only difference is that $L^{\ddagger}$ is the *covariant* form of the differential operator L, for reasons explained in the next section.

Covariant Field Equations. Since the cortex is not a *developable* surface (Davatzikos, 1996), it cannot be given a parameterization whose metric tensor is uniform. As in fluid dynamics or general relativity applications, the intrinsic curvature of the solution domain should be taken into account when computing flow vector fields in the cortical parameter space, and mapping one mesh surface onto another; otherwise errors will arise. The result is *a covariant regularization* approach (Einstein, 1914; Thompson and Toga, 1998; Thompson et al., 1999). From a practical standpoint, this approach uses a mathematical trick that makes it immaterial whether a spherical or planar map is used to simplify the mathematics of cortical matching. Either a spherical or a planar map can be used. Since the flows defined on these maps are adjusted for variations in the metric tensor of the mapping, the results become independent of the underlying parameterization (spherical or planar). In fact, spherical and planar maps involve different amounts of local dilation or contraction of the surface metric, but this metric tensor field is stored and used later to adjust the flow that maps one cortex on another, so which one is used is immaterial. The covariant approach was introduced by Einstein (1914) to allow the solution of physical field equations defined by elliptic operators on manifolds with intrinsic curvature. Similarly, the problem of deforming one cortex onto another involves solving a similar system of elliptic partial differential equations (Drury et al., 1996; Davatzikos, 1996; Thompson and Toga, 1998; Bakircioglu et al., 1999), defined on an intrinsically curved computational mesh (in the shape of the cortex). In the covariant formalism, the differential operators governing the mapping of one cortex to another are adaptively modified to reflect changes in the underlying metric tensor of the surface parameterizations (Fig. 14).

--

Technical Details. Although planar (or spherical) maps serve as proxies for the cortex (Fig. 14), different amounts of local dilation and contraction are required to transform the cortex onto these simpler 2-parameter surfaces. In the covariant tensor approach (Thompson and Toga, 1998), exact information on these metric alterations is stored in the metric tensor of the mapping, $g_{\mathbf{jk}}(\mathbf{r})$. In the subsequent matching procedure, correction terms (Christoffel symbols, $\mathbf{\Gamma^i_{jk}}$) make the necessary adjustments for fluctuations in the metric tensor of the mapping procedure. Since metric distortions caused by mappings to spheres or planes can always be encoded as a metric tensor field, a covariant approach supports comparisons of cortical data using *either* flattened or spherical maps. In the partial differential equation formulation (1), we replace L by the covariant differential operator $L^{\ddagger}$. In $L^{\ddagger}$, all L's partial derivatives are replaced with covariant derivatives. These covariant derivatives are defined with respect to the metric tensor of the surface domain where calculations are performed (*see Footnote 5*).

Footnote 5. The covariant derivative of a (contravariant) vector field, $u^i(\mathbf{x})$, is defined as $u^i_{,k} = \partial u^j/\partial x^k + \mathbf{\Gamma^j_{ik}}\, u^i$ (Thompson and Toga, 1998) where the $\mathbf{\Gamma^j_{ik}}$ are *Christoffel symbols of the second kind* (Einstein, 1914). This expression involves not only the rate of change of the vector field itself, as we move along the cortical model, but also the rate of change of the local basis, which itself varies due to the intrinsic curvature of the cortex. On a surface with no intrinsic curvature, the extra terms (Christoffel symbols) vanish. The Christoffel symbols, expressed in terms of derivatives of the metric tensor components $g_{jk}(\mathbf{x})$, are calculated from the cortical model: $\mathbf{\Gamma^i_{jk}} = (1/2)\, g^{il} (\partial g_{lj}/\partial x^k + \partial g_{lk}/\partial x^j - \partial g_{jk}/\partial x^i)$. Scalar, vector and tensor quantities, in addition to the Christoffel symbols required to implement the diffusion operators on a curved manifold are evaluated by finite differences. These correction terms are then used in the solution of the Dirichlet problem (Joshi et al., 1995) for matching one cortex with another. A final complication is that different metric tensors $g_{jk}(\mathbf{r_p})$ and $h_{jk}(\mathbf{r_q})$ relate (1) the physical domain of the **input** data to the computation mesh (via mapping D_p^{-1}), and (2) the solution on the computation mesh to the **output** data domain (via mapping D_q). To address this problem, two different approaches are possible, using either (1) simultaneous covariant regularization, or (2) Polyakov actions and Beltrami flows (concepts from high-energy physics). In the first approach (Fig. 14), the PDE $L^{\#\#}\mathbf{u}(\mathbf{r_q}) = -\mathbf{F}$ is solved first, to find a flow field $T_{\mathbf{q}}:\mathbf{r}\rightarrow\mathbf{r}-\mathbf{u}(\mathbf{r})$ on the target spherical map with anatomically-driven boundary conditions $\mathbf{u}(\mathbf{r_q}) = \mathbf{u_0}(\mathbf{r_q})$, $\forall \mathbf{r_q} \in M_0 \cup M_1$. Here $L^{\#\#}$ is the covariant adjustment of the differential operator L with respect to the tensor field $h_{jk}(\mathbf{r_q})$ induced by D_q. Next, the PDE $L^{\ddagger}\mathbf{u}(\mathbf{r_p}) = -\mathbf{F}$ is solved, to find a reparameterization $T_{\mathbf{p}}:\mathbf{r}\rightarrow\mathbf{r}-\mathbf{u}(\mathbf{r})$ of the initial spherical map with boundary conditions $\mathbf{u}(\mathbf{r_p}) = \mathbf{0}$, $\forall \mathbf{r_p} \in M_0 \cup M_1$. Here $L^{\ddagger}$ is the covariant adjustment of L with respect to the tensor field $g_{jk}(\mathbf{r_p})$ induced by D_p. The full cortical matching field (Fig. 14, *top right*) is then defined as $\mathbf{x}\rightarrow D_q(F_{pq}(D_p^{-1}(\mathbf{x})))$ with $F_{pq} = (T_{\mathbf{q}})^{-1} \circ (T_{\mathbf{p}})^{-1}$. A second (conceptually related) approach uses Beltrami flows to establish a *p*-harmonic map from one surface to the other. If P and Q are cortical surfaces with metric tensors $g_{jk}(u^i)$ and $h_{jk}(\xi^\alpha)$ defined in local coordinates u^i and ξ^α (i, α=1,2), the energy density of a map between the surfaces $\xi(u)$: $(P,g) \rightarrow (Q,h)$ is the functional $e(\xi):P \rightarrow R$ defined in local coordinates as:

$$e(\xi)(u) = g^{ij}(u)\, \partial\xi^\alpha(u)/\partial u^I\, \partial\xi^\beta(u)/\partial u^j\, h_{\alpha\beta}(\xi(u))$$

The Dirichlet energy of the mapping $\xi(u)$ (i.e. the generalization of the Hilbert space norm to curved spaces) is defined as: $E(\xi) = \int_{\mathbf{P}} e(\xi)(u)\, dP$, where $dP = (\sqrt{\det[g_{ij}]})\, du^1 du^2$. The Euler equations, whose solution $\xi^\alpha(u)$ minimizes the mapping energy, are

$$0 = L(\xi^i) = \Sigma_{m=1 \text{ to } 2} \partial/\partial u^m [(\sqrt{\det[g^{ru}]}) \Sigma_{l=1 \text{ to } 2} g^{ml}_{ur} \partial\xi^i/\partial u^l] \ (i=1,2),$$

(Liseikin, 1991). These equations can be discretized to produce a Beltrami flow (Sochen et al., 1999) or a quasilinear elliptic system (Liseikin, 1991) whose solution is a harmonic map from one surface to the other. This harmonic map (1) minimizes the change in metric from one surface to the other, and (2) is again independent of the parameterizations (spherical or planar) used for each surface.

With this mathematical adjustment, we eliminate the confounding effects of metric distortions that necessarily occur during the mapping procedure. The resulting cortical matching field is independent of the auxiliary mappings (spherical or planar) used to extract it.

Retention of 3D Cortical Information. To ensure that each subject's spherical map can be converted back into a 3D cortical model, cortical surface point position vectors in 3D stereotaxic space are represented on the sphere using a color-code (at 16 bits per channel). This forms an image of the parameter space in RGB color image format (Fig. 14; Thompson and Toga, 1997). To find good matches between cortical regions in different subjects, we first derive a color image map for each respective surface model, and transfer the entire network of sulcal curves back onto it. After performing the matching process using a flow in the parametric space (Fig. 14,15), the corresponding 3D mapping is recovered, carrying one cortex onto another.

IX. Cortical Averaging

The warping field deforming one cortex into gyral correspondence with another can also be used to create an *average* cortex. To do this, all 36 gyral curves for all subjects are first transferred to the spherical parameter space. Next, each curve is uniformly re-parameterized to produce a regular curve of 100 points on the sphere whose corresponding 3D locations are uniformly spaced. A set of 36 average gyral curves for the group is created by vector averaging all point locations on each curve. This *average curve template* (*curves* in Fig. 15(b)) serves as the target for alignment of individual cortical patterns (*cf.* Fischl et al., 1999). Each individual cortical pattern is transformed into the average curve configuration using a flow field within the spherical map (Fig. 15(a),(b)). By carrying a color code (that indexes 3D locations) along with the vector flow that aligns each individual with the average folding pattern, information can be recovered at a particular location in the average folding pattern (Fig. 15(d)) specifying the 3D cortical points mapping each subject to the average. This produces a new coordinate grid on a given subject's cortex (Fig. 15(f)) in which particular grid-points appear in the same location across subjects relative to the mean gyral pattern. By averaging these 3D positions across subjects, an average 3D cortical model was constructed for the group (Fig. 16, *bottom row*). The resulting mapping is guaranteed to average together all points falling on the same cortical locations across the set of brains, and ensures that corresponding features are averaged together.

Cortical Variability. By using the color code (Fig. 15(d)) to identify original cortical locations in 3D space (Fig. 15(f)), displacement fields are recovered mapping each patient into gyrus-by-gyrus correspondence with the average cortex (Fig. 17). Anatomic variability is then defined at each point on the average cortex as the root mean square (r.m.s.) magnitude of the 3D displacement vectors, assigned to each point, in the surface maps driving individuals onto the group average (Thompson et al., 1996a,b, 1997, 1999). This variability pattern is visualized as a color-coded map (Fig. 18).

Overall, variability values rise sharply (Fig. 18) from 4-5 mm in primary motor cortex to localized peaks of maximal variability in posterior perisylvian zones and superior frontal association cortex (16-18 mm). Primary sensory and motor areas show a dramatic, localized invariance (2-5 mm), but variability rises sharply with the transition anteriorly from motor area 4 to prefrontal heteromodal association cortex. Intermediate variability values (6-10 mm) over the inferior prefrontal convexity fall sharply with the transition to archicortical

orbitofrontal cortex, where the gyral pattern is highly conserved across subjects (2-5 mm variability). More laterally, the posterior frontal cortex, including territory occupied by Broca's area, display intermediate variability (6-10 mm). Temporal lobe variability rose from 2-3 mm deep in the Sylvian fissure to 18 mm at the posterior limit of the inferior temporal sulcus in both brain hemispheres, extending into the posterior heteromodal association cortex of the parietal lobe (14-18 mm). When a variety of widely-used registration systems were examined in addition to the Talairach system (Thompson et al., 1999), 3D variability in these higher-order processing areas was consistently a factor of ten greater than the variability in the most highly conserved areas of cortex. The region of maximal variability, in temporal cortex, is tightly linked with the location of human visual area MT (or V5; Watson et al., 1993). This suggests that extreme caution is necessary when referring to activation foci in this important area using stereotaxic coordinates. The overall patterns of variation corroborate recent volumetric findings based on a fine-scale parcellation of the cortex (Kennedy et al., 1998). These studies also suggest a greater morphologic individuality in cortical regions that are phylogenetically more recent.

Tensor Maps of Directional Variation. Structures do not vary to the same degree in every coordinate direction (Thompson et al., 1996), and even these directional biases vary by cortical system. The principal directions of anatomic variability in a group can be shown in a *tensor map* (Figs. 19 and 20). The maps have two uses. First, they make it easier to detect anomalies, which may be small in magnitude but in an unusual direction. Second, they significantly increase the information content of Bayesian priors used for automated structure extraction and identification (Gee et al., 1995; Mangin et al., 1995; Royackkers et al., 1996; Pitiot et al., 1999).

Fig. 19 shows a tensor map of variability for normal subjects, after mapping 20 elderly subjects' data into Talairach space (all right handed, 10 males, 10 females). Rectangular glyphs indicate the principal directions of variation - they are most elongated along directions where anatomic variation is greatest across subjects. Each glyph represents the covariance tensor of the vector fields that map individual subjects onto their group average. Because gyral patterns constrain the mappings, the fields reflect variations in cortical organization at a more local level than can be achieved by only matching global cortical geometry. Note the elongated glyphs in anterior temporal cortex, and the very low variability (in any direction) in entorhinal and inferior frontal areas. By better defining the parameters of allowable normal variations, the resulting information can be leveraged to distinguish normal from abnormal anatomical variants.

Emerging Asymmetries. There is a substantial literature on Sylvian fissure cortical surface asymmetries (Eberstaller, 1884; Cunningham, 1892; Geschwind and Levitsky, 1968; Davidson and Hugdahl, 1994). These asymmetries have been related to functional lateralization (Strauss *et al.*, 1983), handedness (Witelson, 1989), language function (Davidson and Hugdahl, 1994), and asymmetries of associated cytoarchitectonic fields (Galaburda and Geschwind, 1981) and their thalamic projection areas (Eidelberg and Galaburda, 1982). After group averaging of anatomy, asymmetric features emerge that are not observed in individual anatomies due to their considerable variability. As shown in Fig. 18 (*sagittal projection*), the marked anatomic asymmetry in posterior perisylvian cortex (Geschwind and Levitsky, 1968), actually extends rostrally into postcentral cortex, with the posterior bank of the postcentral gyrus thrust forward by 8-9 mm on the right compared to the left. The asymmetry also extends caudally across the lateral convexity into superior and inferior temporal cortex. As shown earlier by averaging ventricular models (Fig. 9), this asymmetry penetrates subcortically into the occipital ventricular horn, but not into adjacent parieto-occipital and calcarine cortex.

The improved ability to localize asymmetry and encode its variability in a disease-specific atlas has interesting applications in schizophrenia (Narr et al., 1999). Schizophrenic patients have anatomic alterations in several brain regions, including the superior temporal gyrus (*e.g.*, Nestor et al., 1993). This gyrus is the approximate site of Wernicke's language area, and marks the *planum temporale* on its superior banks (Geschwind et al., 1985; Galaburda et al., 1990). To focus on language-related cortex in schizophrenic patients, many investigators have

measured the asymmetry of the *planum temporale* and Sylvian fissure in MR images. Nonetheless, studies of these important regions have not always agreed in their findings, with some reporting a lack of asymmetry in schizophrenic patients (Hoff et al., 1992; Kikinis et al., 1994; Petty et al., 1995) and others not (De Lisi et al., 1994; Kleinschmidt et al., 1994; Frangou et al., 1997).

To see if cortical asymmetries were lost in schizophrenia, we made average cortical representations for schizophrenic patients (15 males, all right-handed) and matched controls (also 15 males, right-handed). As described in Section 8, 36 major sulcal curves were used to drive each subject's gyral pattern into a group mean configuration (Fig. 21). The magnitude of anatomic variation in each brain region was also computed from the deformation vector fields, and shown in color as a variability map (Fig. 21, *colors*). Perhaps surprisingly, asymmetry was not attenuated in the patient group. This can be seen immediately in the sagittal projections of average anatomy for each group. Significant asymmetries were confirmed by calculating curvature and extent measures from the parametric mesh models (Narr et al., 1999). In frontal cortex, the patients also displayed greater variability than controls. Since relatively subtle asymmetries emerge clearly in a group atlas, population-based atlases may be advantageous for investigating a variety of alterations in cortical organization or lateralization, and their dependencies on genetic parameters (Kikinis et al., 1994; *cf.* Csernansky et al., 1998; Le Goualher et al., 1999).

Abnormal Asymmetry. In an interesting development, Thirion et al. (1998) applied a warping algorithm to a range of subjects' scans, in each case matching each brain hemisphere with a reflected version of the opposite hemisphere. The resulting asymmetry fields were treated as observations from a spatially-parameterized random vector field, and deviations due to lesion growth or ventricular enlargement were detected using the theory developed in (Thompson et al., 1997). Due to the asymmetric progression of many degenerative disorders (Thompson et al., 1998), abnormal asymmetry may prove to be a sensitive index of pathology in individual subjects or groups. From a more practical standpoint, asymmetry fields are smaller in magnitude than subject-to-subject deformation maps. This makes the fields easier to estimate with automated non-linear registration algorithms (Section 4). When the estimated deformation is small, it is easier to avoid false, non-global minima of the matching measure being optimized.

X. Brain Averaging

Average Image Templates. So far we have described a scheme to create average anatomical models for specific patient groups. By assembling these average models for a wide range of systems (cortex, hippocampus, ventricles, deep sulci, and basal ganglia), an annotated atlas of structures can be built. Nonetheless, before new data to be pooled into the atlas, an average intensity image template is also required that reflects the unique morphology of the diseased population. This makes it easier for automated, intensity-based registration algorithms to align new data with the atlas.

To create a mean image template for a group, several approaches are possible. Which one is used depends on the application objectives. We describe a particular approach, which guarantees that the average template has (1) well-resolved cortical features (Thompson et al., 1999), and (2) the average size and shape for a subject group (Woods et al., 1998). To create an atlas template that is consistent with an average set of anatomical models, high-dimensional model-based registration is required. If scans are mutually aligned with only a linear transformation, the resulting average brain is blurred in the more variable anatomical regions. The resulting average brain also tends to exceed the average dimensions of the component brain images.

By averaging geometric and intensity features separately (*cf.* Ge et al., 1994; Bookstein, 1997; Grenander and Miller, 1998; Thompson et al., 1999), a template can be made with the mean intensity and geometry for a patient

population. We illustrate this approach by using the cortical transformations defined above (Section 9) to create a well-resolved disease-specific image template for an Alzheimer's Disease population.

First, a group of well-characterized Alzheimer's patients was selected, for whom a range of anatomical surface models (84 per brain) had been created in prior morphometric projects (Thompson et al., 1998). An initial image template for the group was constructed by (1) using automated linear transformations (Woods et al., 1993) to align the MRI data with a randomly selected image, (2) intensity-averaging the aligned scans, and then (3) recursively re-registering the scans to the resulting average affine image. The resulting average image was adjusted to have the mean affine shape for the group (Woods et al., 1998). Images and surface models were then linearly aligned to this template, and an average surface set was created for the group (Thompson et al., 1997). Displacement maps (Fig. 22) driving the surface anatomy of each subject into correspondence with the average surface set were then computed, and were extended to the full volume with surface-based elastic warping (see Fig. 7; Thompson and Toga, 1996, 1998). These warping fields reconfigured each subject's 3D image into the average anatomic configuration for the group. By averaging the reconfigured images (after intensity normalization), a crisp image template was created to represent the group (Fig. 23). Note the better-resolved cortical features in the average images after high-dimensional cortical registration. If desired, this AD-specific atlas can retain the coordinate matrix of the Talairach system (with the AC at (0,0,0)) while refining the gyral map of the Talairach atlas to encode the unique anatomy of the AD population. By explicitly computing matching fields that relate gyral patterns across subjects, a well-resolved and spatially consistent set of probabilistic anatomical models and average images can be made to represent the average anatomy and its variation in a subpopulation.

Disease Progression. The templates so far described, for the dementia and schizophrenia populations, have been based on homogeneous patient groups, matched for age, gender, handedness, and educational level. Since AD, in particular, is a progressive disease (see next Section), the initial atlas template was created to reflect a particular stage in the disease (MMSE score: 19.3 +/- 2.0). At this stage, patients often present for initial evaluation, and MR, PET and SPECT scans have maximal diagnostic value. Nonetheless, by expanding the underlying patient database, atlases are under construction to represent the more advanced stages of Alzheimer's disease. By stratifying the population according to different criteria, different atlases can be synthesized to represen other clinically defined groups.

Image Distortion and Registration Accuracy. Since the anatomy of a dementia population is poorly reflected by current imaging templates, substantially less distortion will be applied by mapping multi-modality brain data into an atlas that reflects AD morphology (Mega et al., 1997; Thompson et al., 1998; Woods et al., 1998). Incoming subjects deviate least from the mean template in terms of both image intensity and anatomy. Registration of their imaging data to this template therefore requires minimal image distortion. Since the template has the average affine shape for the group (Woods et al., 1998), least distortion is applied when either linear, non-linear, approaches are used. Interestingly, automated registration approaches were able to reduce anatomic variability to a greater degree if a specially-prepared image template was used as a registration target (Woods et al., 1998; Thompson et al., 1999).

Other Average Templates. Several approaches are under active development to create average brain templates. Many of them are based on high-dimensional image transformations. Average templates have been made for the *Macaque* brain (Grenander and Miller, 1998), and for individual structures such as the *corpus callosum*, (Davatzikos, 1996; Gee et al., 1998), central sulcus (Manceaux-Demiau et al., 1998), cingulate and paracingulate sulci (Paus et al., 1996; Thompson et al., 1997), hippocampus (Haller et al., 1997; Joshi et al., 1998; Csernansky et al., 1998; Thompson et al., 1999) and for transformed representations of the human and *Macaque* cortex (Drury and Van Essen, 1997; Grenander and Miller, 1998; Thompson et al., 1999; Fischl et al.,

1999). Under various metrics, incoming subjects deviate least from these mean brain templates in terms of both image intensity and anatomy. Registration of new data to these templates not only requires minimal image distortion, but also allows faster algorithm convergence. This is because with smaller deformations, non-global minima of the registration measure may be avoided, as the parameter space is searched for an optimal match. For these reasons, templates that reflect the mean geometry and intensity of a group are a topic of active research (Grenander and Miller, 1998; Woods et al., 1998; Thompson et al., 1999).

XI. Dynamic (4D) Brain Atlases

4D Coordinate Systems. Atlasing of data from the developing or degenerating brain presents unique challenges (Toga et al., 1996). However, warping algorithms can be applied to serial scan data to track disease and growth processes in their full spatial and temporal complexity. Maps of anatomical change can be generated by warping scans acquired from the same subject over time (Thirion and Calmon, 1997; Thompson et al., 1998). Serial scanning of human subjects (Fox et al., 1996; Subsol et al., 1997; Freeborough et al., 1998; Thompson et al., 1998) or experimental animals (Jacobs and Fraser, 1994) in a dynamic state of disease or development offers the potential to create 4D models of brain structure. These models incorporate dynamic descriptors of how the brain changes during maturation or disease. They are therefore of interest for investigating and staging brain development. In an atlas setting, these 4-dimensional maps can act as normative data to define aberrant growth rates and their modulation by therapy (Haney et al., 1999).

In our initial human studies (Thompson et al., 1998, 1999), we developed several algorithms to create 4D quantitative maps of growth patterns in the developing human brain. Time-series of high-resolution pediatric MRI scans were analyzed. The resulting tensor maps of growth provided spatially-detailed information on local growth patterns, quantifying rates of tissue maturation, atrophy, shearing and dilation in the dynamically changing brain architecture. Pairs of scans were selected to determine patterns of structural change across the inter-scan interval. Deformation processes recovered by a high-dimensional warping algorithm were then analyzed using vector field operators to produce a variety of tensor maps (Figs. 24). These maps were designed to reflect the magnitude and principal directions of dilation or contraction, the rate of strain, and the local curl, divergence and gradient of flow fields representing the growth processes recovered by the transformation.

The growth maps obtained in these studies exhibit several striking characteristics. First, foci of rapid growth at the callosal isthmus appeared consistently across puberty. These rates appeared to attenuate as subjects progressed into adolescence (Fig. 24). Rapid rates of tissue loss were also revealed at the head of the caudate, in an earlier phase of development (Fig. 25).

In the near future, 4D atlases will be map growth and degeneration in their full spatial and temporal complexity. Despite the logistic and technical challenges, these mapping approaches hold tremendous promise in analyzing the dynamics of degenerative or neoplastic diseases. They will ultimately play a role in detecting how different therapeutic approaches modulate the course of disease.

XII. Conclusion

Encoding patterns of anatomical variation in disease presents significant challenges. By describing an atlasing scheme that treats intensity and geometric variation separately, we described the creation of well-resolved image templates and probabilistic models of anatomy that reflect the average morphology of a group. The continual refinement of anatomic templates is likely to be leveraged by algorithms for deformation-based morphometry in

large image databases (Thompson et al., 1997; Ashburner et al., 1998), and by next-generation probabilistic atlases. Atlas data on anatomic variability can also act as Bayesian prior information to guide algorithms for automated image registration and labeling (Gee et al., 1998; Ashburner et al., 1998; Pitiot et al., 1999). The resulting atlases are expandable in every respect, and may be stratified into subpopulations according to clinical, demographic or genetic criteria.

We also described approaches for creating and averaging brain models. These techniques produce statistical maps of group differences, abnormalities, and patterns of variation and asymmetry. These maps and models are key components of disease-specific brain atlases. We also described registration algorithms that transfer *post mortem* maps into an atlas, to correlate them with functional and metabolic data. The result is a multi-modality atlas that relates cognitive and functional measures with the cellular and pathologic hallmarks of the disease (Fig. 1; Mega et al., 1997).

As well as disease-specific atlases reflecting brain structure in dementia and schizophrenia (Thompson et al., 1999; Narr et al., 1999), research is underway to build dynamic brain atlases that retain probabilistic information on growth rates in development and degeneration (Thompson et al., 1999). Refinement of these atlas systems to support dynamic and disease-specific data should generate an exciting framework to investigate variations in brain structure and function in large human populations.

…….

Acknowledgments

This work was supported by research grants from the National Center for Research Resources (P41 RR13642 and RR05956), the National Institute of Neurological Disorders and Stroke and the National Institute of Mental Health (NINDS/NIMH NS38753), and by a *Human Brain Project* grant to the International Consortium for Brain Mapping, funded jointly by NIMH and NIDA (P20 MH/DA52176). Additional support was also provided by the United States Information Agency (Grant G-1-00001), Howard Hughes Medical Institute, and U.S.-U.K. Fulbright Commission, and by the National Library of Medicine (LM/MH05639) and National Science Foundation (BIR 93-22434). Special thanks go to our colleagues Roger Woods, Colin Holmes, Jay Giedd, David MacDonald, Alan Evans, and John Mazziotta, whose advice and support have been invaluable in these investigations.

……..

References

Amit Y, Grenander U, Piccioni M (1991). *Structural Image Restoration through Deformable Templates*, J. Amer. Stat. Assoc., 86(414):376-386.

Amunts K, Schlaug G, Schleicher A, Steinmetz H, Dabringhaus A, Roland PE, Zilles K (1996). Asymmetry in the human motor cortex and handedness. Neuroimage 1996 Dec;4(3 Pt 1):216-22 .

Andreasen NC, Arndt S, Swayze V, Cizadlo T, Flaum M, O'Leary D, Ehrhardt JC, Yuh WTC (1994). Thalamic Abnormalities in Schizophrenia Visualized through Magnetic Resonance Image Averaging, Science, 14 October 1994, 266:294-298.

Arnold SE, Hyman BT, Flory J, Damasio AR, Van Hoesen GW (1991). *The Topographical and Neuroanatomical Distribution of Neurofibrillary Tangles and Neuritic Plaques in the Cerebral Cortex of Patients with Alzheimer's Disease*, Cerebral Cortex 1:103-116.

Ashburner J, Neelin P, Collins DL, Evans AC, Friston KJ (1997). *Incorporating Prior Knowledge into Image Registration*, Neuroimage 6(4):344-352.

Ashburner J, Hutton C, Frackowiak R, Johnsrude I, Price C, Friston K (1998). Identifying global anatomical differences: deformation-based morphometry. Hum Brain Mapp 1998;6(5-6):348-57.

Aso M, Kurachi M, Suzuki M, Yuasa S, Matsui M, Saitoh O (1995). *Asymmetry of the ventricle and age at the onset of schizophrenia*. European Arch. of Psych. and Clin. Neurosci., 245(3):142-4.

Aylward EH, Harris GJ, Hoehn-Saric R, Barta PE, Machlin SR, Pearlson GD (1996). Normal caudate nucleus in obsessive-compulsive disorder assessed by quantitative neuroimaging.Arch Gen Psychiatry 1996 Jul;53(7):577-84.
Bajcsy R, Kovacic S (1989). Multiresolution Elastic Matching, Computer Vision, Graphics and Image Processing, 46:1-21.
Bakircioglu M, Joshi SC, Miller MI (1999). Landmark Matching on Brain Surfaces Via Large Deformation Diffeomorphisms on the Sphere, Proc. SPIE Medical Imaging 1999.
Baumgardner TL, Singer HS, Denckla MD, Rubin BS, Abrams BA, Colli MJ, Reiss AL (1996) Corpus callosum morphology in children with Tourette syndrome and attention deficit hyperactivity disorder. Neurology, 47:477-482.
Beaton AA: The relation of planum temporale asymmetry and morphology of the corpus callosum to handedness, gender and dyslexia: a review of the evidence. Brain and Language 1997;60:255-322.
Berg L, McKeel DW Jr, Miller JP, Baty J, Morris JC (1993) Neuropathological indexes of Alzheimer's disease in demented and nondemented persons aged 80 years and older. Arch Neurol 1993 Apr;50(4):349-58.
Bilder RM, Wu H, Chakos MH, Bogerts B, Pollack S, Aronowitz J, Ashtari M, Degreef G, Kane JM, Lieberman JA (1994). Cerebral morphometry and clozapine treatment in schizophrenia. J Clin Psychiatry 1994 Sep;55 Suppl B:53-6 .
Bishop KM, Wahlsten, D: Sex differences in the human corpus callosum: myth of reality? Neuroscience and Biobehavioral Reviews 1997;21:581-601.
Blanton RE, Levitt J, Thompson PM, Badrtalei S, Capetillo-Cunliffe L, Toga AW (1999). *Average 3-Dimensional Caudate Surface Representations in a Juvenile-Onset Schizophrenia and Normal Pediatric Population*, Presentation #621, 5th International Conference on Functional Mapping of the Human Brain, Dusseldorf, Germany, June 1999.
Bohm C, Greitz T, Kingsley D, Berggren BM, Olsson L (1983). Adjustable Computerized Brain Atlas for Transmission and Emission Tomography, Am. J. Neuroradiol. 4:731-733.
Bookstein FL (1997). Landmark Methods for Forms Without Landmarks: Morphometrics of Group Differences in Outline Shape, Medical Image Analysis 1(3):225-243.
Braak H, Braak E (1991). *Neuropathological Staging of Alzheimer-Related Changes*, Acta Neuropathol. 82:239-259.
Brodmann K (1909). Vergleichende Lokalisationslehre der Grosshirnrinde in ihren Prinzipien dargestellt auf Grund des Zellenbaues, Barth, Leipzig, In: Some Papers on the Cerebral Cortex, translated as: On the Comparative Localization of the Cortex, 201-230, Thomas, Springfield, IL, 1960.
Broit C (1981). Optimal Registration of Deformed Images, PhD Dissertation, Univ. of Pennsylvania, USA.
Bro-Nielsen M, Gramkow C (1996). Fast Fluid Registration of Medical Images, In: Höhne KH, Kikinis R [eds.], Visualization in Biomedical Computing, Hamburg, Germany, Lecture Notes in Computer Science 1131:267-276, Springer Verlag, Berlin.
Brun A, Englund E (1981). *Regional Pattern of Degeneration in Alzheimer's Disease: Neuronal Loss and Histopathologic Grading*, Histopathology 5:549-564.
Burke HL, Yeo RA, Delaney HD, Conner L (1993). CT scan cerebral hemispheric asymmetries: predictors of recovery from aphasia. J Clin Exp Neuropsychol 1993 Mar;15(2):191-204.
Cao J, Worsley KJ (1999). The Geometry of the Hotelling's T-squared Random Field with Applications to the Detection of Shape Changes, Annals of Statistics, [in press].
Carpenter WT, Buchanan RW, Kirkpatrick B, Tamminga C, Wood F: Strong inference, theory testing, and the neuroanatomy of schizophrenia. Arch of Gen Psychiatry 1993;50:825-831.
Cassanova MF, Sanders RD, Goldberg TE, Bigelow LB, Christison G, Torrey EF, Weinberger DR: Morphometry of the corpus callosum in monozygotic twins discordant for schizophrenia: a magnetic resonance imaging study. J Neurology, Neurosurgery and Psychiatry 1990;53:416-21.
Castellanos FX, Giedd JN, Marsh WL, Hamburger SD, Vaituzis AC, Dickstein DP, Sarfatti SE, Vauss YC, Snell JW, Lange N, Kaysen D, Krain AL, Ritchie GF, Rajapakse JC, Rapoport JL (1996). Quantitative brain Magnetic resonance imaging in attention-deficit hyperactivity disorder.Arch Gen Psychiatry 1996 Jul;53(7):607-16.
Chakos MH, Lieberman JA, Bilder RM, Borenstein M, Lerner G, Bogerts B, Wu H, Kinon B, Ashtari M (1994). Increase in caudate nuclei volumes of first-episode schizophrenic patients taking antipsychotic drugs. Am J Psychiatry 1994 Oct;151(10):1430-6.
Christensen GE, Rabbitt RD, Miller MI (1993). A Deformable Neuroanatomy Textbook based on Viscous Fluid Mechanics, 27th Ann. Conf. on Inf. Sciences and Systems, 211-216.
Christensen GE, Miller MI, Marsh JL, Vannier MW (1995). Automatic Analysis of Medical Images using a Deformable Textbook, Proc. Comp. Assist. Radiol. 1995, Springer, Berlin, 152-157.
Christensen GE, Rabbitt RD, Miller MI, Joshi SC, Grenander U, Coogan TA, Van Essen DC (1995). Topological Properties of Smooth Anatomic Maps, in: Bizais Y, Barillot C, Di Paola R [eds.], Information Processing in Medical Imaging, June 1995, 101-112.
Christensen GE, Rabbitt RD, Miller MI (1996). Deformable Templates using Large Deformation Kinematics, IEEE Trans. on Image Processing, Oct. 1996, 5(10):1435-1447.
Clarke JM, Zaidel E: Anatomical-behavioral relationships: corpus callosum morphometry and hemispheric specialization. Behavioral Brain Research 1994;64:185-202.
Clarke S, Kraftsik R, Van der Loos H, Innocenti GM (1989) Forms and measures of adult and developing human corpus callosum. Journal of Neuropathology and Experimental Neurology, 280: 213-230.
Cohen LD, Cohen I (1992). *Deformable Models for 3D Medical Images using Finite Elements & Balloons*, in: Proceedings: 1992 IEEE Computer Society Conference on Computer Vision and Pattern Recognition (Cat. No. 92CH3168-2), Los Alamitos, CA, USA. IEEE Comput. Soc. Press, 592-8.
Cook MJ, Free SL, Fish DR, Shorvon SD, Straughan K, Stevens JM (1994). *Analysis of Cortical Patterns*, In: *Magnetic Resonance Scanning and Epilepsy* (Shorvon SD, ed), 263-274. New York: Plenum.

Collins DL, Neelin P, Peters TM, Evans AC (1994a). Automatic 3D Intersubject Registration of MR Volumetric Data into Standardized Talairach Space, J. Comp. Assisted Tomography, March 1994, 18(2):192-205.
Collins DL, Peters TM, Evans AC (1994b). An Automated 3D Non-Linear Image Deformation Procedure for Determination of Gross Morphometric Variability in the Human Brain, Proc. Visualization in Biomed. Comp. (SPIE) 3:180-190.
Collins DL, Holmes CJ, Peters TM, Evans AC (1995). Automatic 3D Model-Based Neuroanatomical Segmentation, Human Brain Mapping 3:190-208.
Collins DL, Le Goualher G, Venugopal R, Caramanos A, Evans AC, Barillot C (1996). Cortical Constraints for Non-Linear Cortical Registration, In: Höhne KH, Kikinis R, [eds.], Visualization in Biomedical Computing, Hamburg, Germany, Sept. 1996, Lecture Notes in
Computer Science, 1131:307-316, Springer Verlag, Berlin.
Colombo C, Bonfanti A, Livian S, Abbruzzese M, Scarone S: Size of the corpus callosum and auditory comprehension in schizophrenics and normal controls. Schizophrenia Research 1993;11:1:63-70.
Courchesne E, Saitoh O, Yeung-Courchesne R, Press GA, Lincoln AJ, Haas RH, Schreibman L (1994). Abnormality of cerebellar vermian lobules VI and VII in patients with infantile autism: identification of hypoplastic and hyperplastic subgroups with MR imaging. AJR Am J Roentgenol 1994 Jan;162(1):123-30.
Courchesne E (1997). Brainstem, cerebellar and limbic neuroanatomical abnormalities in autism. Curr Opin Neurobiol 1997 Apr;7(2):269-278.
Csernansky JG, Joshi S, Wang L, Haller JW, Gado M, Miller JP, Grenander U, Miller MI (1998*). Hippocampal morphometry in schizophrenia by high dimensional brain mapping*. Proc Natl Acad Sci U S A 1998 Sep 15;95(19):11406-11.
Cuénod CA, Denys A, Michot JL, Jehenson P, Forette F, Kaplan D, Syrota A, Boller F (1993). *Amygdala Atrophy in Alzheimer's Disease: An In Vivo Magnetic Resonance Imaging Study*, Arch. Neurol. 50:941-945.
Cunningham DJ (1892). *Contribution to the Surface Anatomy of the Cerebral Hemispheres*, Cunningham Memoirs (R. Irish Acad.) 7:372.
Dale AM, Sereno MI (1993). *Improved Localization of Crtical Activity by Combining EEG and MEG with MRI Cortical Surface Reconstruction - A Linear Approach*, 5(2):162-176.
Davatzikos C (1996a). Spatial Normalization of 3D Brain Images using Deformable Models, J. Comp. Assisted Tomography 20(4):656-665, Jul.-Aug. 1996.
Davatzikos C, Vaillant M, Resnick SM, Prince JL, Letovsky S, Bryan RN (1996b). A Computerized Approach for Morphological Analysis of the Corpus Callosum, J. Comp. Assisted Tomography, 20(1):88-97.
Davidson RJ, Hugdahl K (1994). *Brain Asymmetry*, MIT Press.
Dengler J, Schmidt M (1988). *The Dynamic Pyramid - A Model for Motion Analysis with Controlled Continuity*, Int. J. Patt. Recogn. and Artif. Intell. 2(2):275-286.
DeLacoste-Utamsing MC, Holloway RL: Sexual dimorphism in the human corpus callosum. Science 1982;216:1431-1432.
DeLisi LE, Dauphinais ID, Hauser P: Gender differences in the brain: are they relevant to the pathogenesis of schizophrenia? Compar Psychiatry 1989;30:197-208.
DeLisi LE, Hoff AL, Neale C, Kushner M: Asymmetries in the superior temporal lobe in male and female first-episode schizophrenic patients: measures of the planum temporale and superior temporal gyrus by MRI. Schizophrenia Res 1994;12:19-28.
DeQuardo JR, Bookstein FL, Green WD, Brunberg JA, Tandon R (1996). Spatial Relationships of Neuroanatomic Landmarks in Schizophrenia, Psychiatry Research 67(1): 81-95.
Dinov ID, Thompson PM, Woods RP, Mega MS, Holmes CJ, Sumners D, Saxena S, Toga AW (1999) Probabilistic Sub-Volume Partitioning Techniques for Determining the Statistically Significant Regions of Activation in Stereotaxic Functional Data, [in press]..
Drury HA, Van Essen DC, Joshi SC, Miller MI (1996). Analysis and Comparison of Areal Partitioning Schemes Using Two-Dimensional Fluid Deformations, Poster Presentation, 2nd Int. Conf. on Functional Mapping of the Human Brain, Boston, Massachusetts USA, June 17-21 1996, NeuroImage 3:S130.
Drury HA, Van Essen DC (1997) Analysis of Functional Specialization in Human Cerebral Cortex using the Visible Man Surface Based Atlas, Human Brain Mapping 5:233-237.
Dupuis P, Grenander U, Miller MI (1998) Variational problems on flows of diffeomorphisms for image matching. QUARTERLY OF APPLIED MATHEMATICS, 1998 SEP, V56 N3:587-600.
Eberstaller O (1884). *Zür Oberflachen Anatomie der Grosshirn Hemisphaeren*, Wien Med. Bl., 7:479,642,644.
Eidelberg D, Galaburda AM (1982). *Symmetry and Asymmetry in the Human Posterior Thalamus: I. Cytoarchitectonic Analysis in Normal Persons*, Arch. Neurol. 39(6):325-332.
Einstein A (1914). *Covariance Properties of the Field Equations of the Theory of Gravitation Based on the Generalized Theory of Relativity*, 29 May 1914, published as *Kovarianzeigenschaften der Feldgleichungen der auf die verallgemeinerte Relativitätstheorie gegründeten Gravitationstheorie*, Zeitschrift für Mathematik und Physik 63 (1914): 215-225
Erkinjuntti T, Lee DH, Gao F, Steenhuis R, Eliasziw M, Fry R, Merskey H, Hachinski VC (1993). *Temporal Lobe Atrophy on Magnetic Resonance Imaging in the Diagnosis of Early Alzheimer's Disease,* Arch. Neurol. 50(3):305-310.
Evans AC, Dai W, Collins DL, Neelin P, Marrett S (1991). Warping of a Computerized 3D Atlas to Match Brain Image Volumes for Quantitative Neuroanatomical and Functional Analysis, SPIE Med. Imaging 1445:236-247.
Evans AC, Collins DL, Milner B (1992). An MRI-based Stereotactic Brain Atlas from 300 Young Normal Subjects, in: Proceedings of the 22nd Symposium of the Society for Neuroscience, Anaheim, 408.
Evans AC, Collins DL, Neelin P, MacDonald D, Kamber M, Marrett TS (1994). Three-Dimensional Correlative Imaging: Applications in Human Brain Mapping, in: Functional Neuroimaging: Technical Foundations, Thatcher RW, Hallett M, Zeffiro T, John ER, Huerta M [eds.], 145-162.

Falkai P, Bogerts B, Greve B, Pfeiffer U, Machus B, Folsch-Reetz B, Majtenyi C, Ovary I (1992). Loss of sylvian fissure asymmetry in schizophrenia. A quantitative post mortem study. Schizophr Res 1992 Apr;7(1):23-32.

Filipek PA (1995). Quantitative magnetic resonance imaging in autism: the cerebellar vermis. Curr Opin Neurol 1995 Apr;8(2):134-8 .

Filipek PA (1995). Brief report: neuroimaging in autism: the state of the science 1995. J Autism Dev Disord 1996 Apr;26(2):211-5.

Fischl B, Sereno MI, Tootell RBH, Dale AM (1999). High-Resoltuion Inter-Subject Averaging and a Coordinate System for the Cortical Surface, [in press].

Fox NC, Freeborough PA, Rossor MN (1996). *Visualization and Quantification of Rates of Cerebral Atrophy in Alzheimer's Disease*, Lancet 348(9020):94-97, Jul. 1996.

Fox PT, Perlmutter JS, Raichle M (1985). A Stereotactic Method of Localization for Positron Emission Tomography, J. Comp. Assist. Tomogr. 9(1):141-153.

Fox PT, Mintun MA, Reiman EM, Raichle ME (1988). Enhanced Detection of Focal Brain Responses using Inter-Subject Averaging and Change Distribution Analysis of Subtracted PET Images, J. Cereb. Blood Flow Metab. 8:642-653.

Fox PT, Mikiten S, Davis G, Lancaster JL (1994). BrainMap: A Database of Human Functional Brain Mapping, in: Functional Neuroimaging: Technical Foundations, Thatcher RW, Hallett M, Zeffiro T, John ER, Huerta M [eds.], 95-106.

Frangou S, Sharma t, Sigmudsson T, Barta P, Pearlson G, Murray RM: The Maudsley Family study.4: Normal planum temporale asymmetry in familial schizophrenia: a volumetric MRI study. Br J of Psychiatry 1997;170:230-33.

Freeborough PA, Woods RP, Fox NC (1996). *Accurate Registration of Serial 3D MR Brain Images and its Application to Visualizing Change in Neurodegenerative Disorders*, J. Comput. Assist. Tomogr. 20(6):1012-1022, Nov. 1996.

Friedland RP, Luxenberg J (1988). *Neuroimaging and Dementia*, in: *Clinical Neuroimaging: Frontiers in Clinical Neuroscience*, vol. 4, Theodore WH [ed.], Allan Liss, Inc., New York, 139-163.

Friston KJ, Passingham RE, Nutt JG, Heather JD, Sawle GV, Frackowiak RSJ (1989). Localization in PET Images: Direct Fitting of the Intercommissural (AC-PC) Line, J. Cereb. Blood Flow Metab. 9:690-695.

Friston KJ, Frith CD, Liddle PF, Frackowiak RSJ (1991). Plastic Transformation of PET Images, J. Comp. Assist. Tomogr. 9(1):141-153.

Friston KJ, Holmes AP, Worsley KJ, Poline JP, Frith CD, Frackowiak RSJ (1995). Statistical Parametric Maps in Functional Imaging: A General Linear Approach, Human Brain Mapping 2:189-210.

Fuh JL, Mega MS, Thompson PM, Cummings JL, Toga AW (1997) *Cortical Complexity Maps and Cognition in Alzheimer's Disease,* Proc. 122nd Annual Meeting of the American Neurological Association, 1997.

Gabrani M, Tretiak OJ (1999). *Surface-based matching using elastic transformations*, Pattern Recognition, 32(1):87-97.

Galaburda AM, Geschwind N (1981). *Anatomical Asymmetries in the Adult and Developing Brain and their Implications for Function,* Adv. Pediatr. 28:271-292.

Galaburda AM, Rosen GD, Sherman GF: Individual variability in cortical organization: its relationship to brain laterality and implications to function, Neuropsychologica 1990;28:529-546.

Gaser C, Kiebel S, Riehemann S, Volz H-P, Sauer H (1998). Statistical parametric mapping of structural changes in brain - Application to schizophrenia research, Poster #0718, 4th Int. Conf. on Functional Mapping of the Human Brain, Montreal, 1998.

Ge Y, Fitzpatrick JM, Kessler RM, Jeske-Janicka M (1995). *Intersubject Brain Image Registration using both Cortical and Subcortical Landmarks*, SPIE Image Processing 2434:81-95.

Gee JC, Reivich M., Bajcsy R (1993). Elastically Deforming an Atlas to Match Anatomical Brain Images, J. Comp. Assist. Tomogr. 17(2):225-236, March 1993.

Gee JC, LeBriquer L, Barillot C, Haynor DR, Bajcsy R (1995). Bayesian Approach to the Brain Image Matching Problem, Inst. for Res. in Cogn. Sci. Technical Report 95-08, April 1995.

Gee JC, Bajscy RK (1998). *Elastic Matching: Continuum-Mechanical and Probabilistic Analysis*, in: Toga AW [ed.], Brain Warping, Academic Press, San Diego.

Geschwind N, Levitsky W (1968). Human Brain: Left-Right Asymmetries in Temporal Speech Region, Science 161: 186.

Geschwind N, Galaburda AM, Cerebral lateralization. Biological mechanisms, associations and pathology. Arch Neurology 1985;428-459.

Giedd JN, Castellanos FX, Casey BJ, Kozuch P, King AC, Hamburger SD, Rapaport JL (1994) Quantitative morphology of the corpus callosum in attention deficit hyperactivity disorder. American Journal of Psychiatry, 151: 665-669.

Giedd JN, Rumsey JM, Castellanos FX, Rajapakse JC, Kaysen D, Vaituzis AC, Vauss AC, Hamburger SD, Rapoport JL (1996) A quantitative MRI study of the corpus callosum in children and adolescents. Developmental Brain Research, 91: 274-280.

Gramkow C (1996) *Registration of 2D and 3D Medical Images*, Denmark Tech. Univ. M.Sc. Thesis, 1996.

Greitz T, Bohm C, Holte S, Eriksson L (1991). A Computerized Brain Atlas: Construction, Anatomical Content and Application, J. Comp. Assist. Tomogr. 15(1):26-38.

Grenander U (1976). *Pattern Synthesis: Lectures in Pattern Theory*, Applied Math. Sci. 13, Springer-Verlag.

Grenander U, Miller MI (1994). Representations of Knowledge in Complex Systems, J. Royal Statistical Society B, 56(4):549-603.

Grenander U, Miller MI (1998). Computational Anatomy: An Emerging Discipline, Technical Report, Dept. of Mathematics, Brown University.

Haller JW, Banerjee A, Christensen GE, Gado M, Joshi S, Miller MI, Sheline Y, Vannier MW, Csernansky JG (1997). Three-Dimensional Hippocampal MR Morphometry with High-Dimensional Transformation of a Neuroanatomic Atlas, Radiology, Feb. 1997, 202(2):504-510.

Haney S, Thompson PM, Alger JR, Cloughesy TF, Toga AW (1999). *Tracking Tumor Growth Rates in Patients with Malignant Gliomas*, 4th Annual Meeting of the Society for Neuro-Oncology, Scottsdale, AZ, Nov. 1999.

Hardy TL (1994). Computerized Atlas for Functional Stereotaxis, Robotics and Radiosurgery, SPIE Vol. 2359:447-456.
Harrison PJ (1999). The neuropathology of schizophrenia. A critical review of the data and their interpretation.Brain. 1999 Apr;122 (Pt 4):593-624.
Hegedüs K, Molnár P (1996). Neuroanatomy and Neuropathology on the Internet, Department of Neurology, University Medical School, Debrecen, Hungary, http://www.neuropat.dote.hu/
Hoff AL, Roidan H, O'Donnell D, Stritzke P, Neale C, Boccio A, Anand AK, DeLisi LE: Anomalous lateral sulcus asymmetry and cognitive function in first-episode schizophrenia. Schizophrenia Bull 1992;18:2:257-270.
Höhne KH, Bomans M, Pommert A, Riemer M, Schiers C, Tiede U, Wiebecke G (1990). 3D Visualization of Tomographic Volume Data using the Generalized Voxel Model, Visual Comput. 6:28-36.
Höhne KH, Bomans M, Riemer M, Schubert R, Tiede U, Lierse W (1992). A 3D Anatomical Atlas Based on a Volume Model, IEEE Comput. Graphics Appl. 12:72-78.
Holman LB, Chandak PK, Garada BM (1994). Atlas of Brain Perfusion SPECT, http://brighamrad.harvard.edu/education/online/BrainSPECT/BrSPECT.html
Hynd GW, Semrud-Clikeman M, Lorys AR, Novey ES, Eliopulos D, Lyytinen J (1991) Corpus callosum morphology in attention deficit hyperactivity disorder: morphometric analysis of MRI. Journal of Learning Disabilities, 24:141-146.
Ingvar M, Eriksson L, Greitz T, Stoneelander S et al., (1994). *Methodological Aspects of Brain Activation Studies - Cerebral Blood Flow Determined with [O-15]-Butanol and Positron Emission Tomography*, J. Cereb. Blood Flow and Metab. 14(4):628-638, Jul. 1994.
Iosifescu DV, Shenton ME, Warfield SK, Kikinis R, Dengler J, Jolesz FA, McCarley RW (1997). An Automated Registration Algorithm for Measuring MRI Subcortical Brain Structures, NeuroImage, Jul. 1997, 6(1):13-25.
Jack CR Jr (1994). MRI-based hippocampal volume measurements in epilepsy. Epilepsia 1994;35 Suppl 6:S21-9.
Jacobs RE, Fraser SE (1994). *Magnetic Resonance Microscopy of Embryonic Cell Lineages and Movements*, Science, 263(5147):681-684.
Jäncke L, Staiger JF, Schlaug G, Huang Y, Steinmetz H: The relationship between corpus callosum size and forebrain volume. Cerebral Cortex 1997:7;1047-3211.
Jenike MA, Breiter HC, Baer L, Kennedy DN, Savage CR, Olivares MJ, O'Sullivan RL, Shera DM, Rauch SL, Keuthen N, Rosen BR, Caviness VS, Filipek PA (1996). Cerebral structural abnormalities in obsessive-compulsive disorder. Aquantitative morphometric magnetic resonance imaging study. Arch Gen Psychiatry 1996 Jul;53(7):625-32.
Jernigan TL, Salmon DP, Butters N, Hesselink JR (1991). *Cerebral Structure on MRI: Part I. Localization of Age-Related Changes*, Biol. Psychiatry 29:55-67.
Jernigan TL, Bellugi U, Sowell E, Doherty S, Hesselink JR (1993) Cerebral morphological distinctions between Williams and Down Syndromes. Archives of Neurology, 50:186-191.
Johnson KA (1996). The Harvard Whole Brain Atlas, http://www.med.harvard.edu/AANLIB/home.html
Johnson VP, Swayze VW, Sato Y, Andreason NC (1996) Fetal alcohol syndrome: craniofacial and central nervous system manifestations. American Journal of Medical Genetics, 61:329-339.
Joshi SC, Miller MI, Christensen GE, Banerjee A, Coogan TA, Grenander U (1995). Hierarchical Brain Mapping via a Generalized Dirichlet Solution for Mapping Brain Manifolds, Vision Geometry IV, Proc. SPIE Conference on Optical Science, Engineering and Instrumentation, San Diego, CA, Aug. 1995, 2573:278-289.
Joshi S, Miller MI, Grenander U (1998). *On the Geometry and Shape of Brain Sub-Manifolds*, Int. J. Patt. Recogn. and Artif. Intell. [in press].
Kennedy DN, Lange N, Makris N, Bates J, Meyer J, Caviness VS Jr. (1998). Gyri of the human neocortex: an MRI-based analysis of volume and variance. Cerebral Cortex, 1998 Jun, 8(4):372-84.
Kido DK, Caine ED, LeMay M, Ekholm S, Booth H, Panzer R (1989). *Temporal Lobe Atrophy in Patients with Alzheimer Disease: A CT Study*, AJNR 7:551-555.
Killiany RJ, Moss MB, Albert MS, Sandor T, Tieman J, Jolesz F (1993). *Temporal Lobe Regions on Magnetic Resonance Imaging Identify Patients with Early Alzheimer's Disease*, Arch. Neurol. 50:949-954.
Kikinis R, Shenton ME, Gerig G, Hokama H, Haimson J, O'Donnell BF, Wible CG, McCarley RW, Jolesz FA (1994). *Temporal Lobe Sulco-Gyral Pattern Anomalies in Schizophrenia: An in vivo MR Three-Dimensional Surface Rendering Study*, Neuroscience Letters 182:7-12.
Kikinis R, Shenton ME, Iosifescu DV, McCarley RW, Saiviroonporn P, Hokama HH, Robatino A, Metcalf D, Wible CG, Portas CM, Donnino R, Jolesz F (1996). A Digital Brain Atlas for Surgical Planning, Model-Driven Segmentation, and Teaching, IEEE Trans. on Visualization and Comp. Graphics, Sept. 1996, 2(3):232-241.
Kim B, Boes JL, Frey KA, Meyer CR (1997). *Mutual Information for Automated Unwarping of Rat Brain Autoradiographs*, Neuroimage 5(1):31-40.
Kjems U, Strother SC, Anderson J, Law I, Hansen LK (1999). Enhancing the multivariate signal of [15O] water PET studies with a new nonlinear neuroanatomical registration algorithm. IEEE Trans Med Imaging 1999 Apr;18(4):306-19.
Kleinschmidt A, Falkai P, Huang Y, Schneider T, Furst G, Steinmetz H: In vivo morphometry of planum temporale asymmetry in first-episode schizophrenia. Schizophrenia Res 1994;12:9-18.
Kwong EM, Mega MS, Thompson PM, Xu LQ, Ercoli LM, Cummings JL, Small GW, Felix J, Toga AW (1999). *Three-Dimensional Hippocampal Maps In Normal Aging, Older Persons with Mild Cognitive Impairment and Patients with Alzheimer's Disease*, Annual Conference of the American Academy of Neurology, 1999.
Lawrie SM, Abukmeil SS: Brain abnormality in schizophrenia. Br J of Psychiatry 1998;172:110-120.
Lee MA, Smith S, Palace J, Matthews PM (1998). Defining multiple sclerosis disease activity using MRI T2-weighted difference imaging. Brain 1998 Nov;121 (Pt 11):2095-102 .

Lee MA, Smith S, Palace J, Narayanan S, Silver N, Minicucci L, Filippi M, Miller DH, Arnold DL, Matthews PM (1999). Spatial mapping of T2 and gadolinium-enhancing T1 lesion volumes in multiple sclerosis: evidence for distinct mechanisms of lesion genesis? Brain 1999 Jul;122(Pt 7):1261-1270.
Le Goualher G, Procyk E, Collins DL, Venugopal R, Barillot C, Evans AC (1999) Automated extraction and variability analysis of sulcal neuroanatomy, IEEE Trans Med Imaging 1999 Mar;18(3):206-17
Leonard CM (1996). *Structural Variation in the Developing and Mature Cerebral Cortex: Noise or Signal?*, in: *Developmental Neuroimaging: Mapping the Development of Brain and Behavior*; [eds:] Thatcher RW, Reid Lyon G, Rumsey J, Krasnegor N, Academic Press, 207-231.
Lester H, Arridge SR, Jansons KM, Lemieux L, Hajnal JV, Oatridge A (1999). *Non-linear registration with the variable viscosity fluid algorithm*, 16th Int. Conf. on Info. Proc. in Med. Imaging, IPMI'99 [in press].
Liseikin VD (1991). On a Variational Method for Generating Adaptive Grids on N-Dimensional Surfaces, Doklady Akademii Nauk. CCCP, 1991, V319 N3:546-549.
Loewenstein DA, Barker WW, Chang JY, Apicella A, Yoshii F, Kothari P, Levin B, Duara R (1989). *Predominant Left Hemisphere Metabolic Dysfunction in Dementia*, Arch. Neurol. 46(2):146-152.
Lyoo IK, Noam GG, Chang KL, Ho KL, Kennedy BP, Renshaw PF (1996) The corpus callosum and lateral ventricles in children with attention deficit hyperactivity disorder: a brain magnetic resonance imaging study. Biological Psychiatry, 40:1060-1063.
MacDonald D, Avis D, Evans AC (1993). Automatic Parameterization of Human Cortical Surfaces, Annual Symp. Info. Proc. in Med. Imag., (IPMI).
Mai J, Assheuer J, Paxinos G (1997). Atlas of the Human Brain, Academic Press.
Manceaux-Demiau A, Bryan RN, Davatzikos C (1998). *A Probabilistic Ribbon Model for Shape Analysis of the Cerebral Sulci: Application to the Central Sulcus*, J. Comp. Assist. Tomogr. [in press].
Mangin J-F, Frouin V, Bloch I, Regis J, Lopez-Krahe J (1994). *Automatic Construction of an Attributed Relational Graph Representing the Cortex Topography using Homotopic Transformations*, SPIE 2299, 110-121.
Mansour A, Fox CA, Burke S, Akil H, Watson SJ (1995). Immunohistochemical Localization of the Cloned Mu Opioid Receptor in the Rat CNS, J. Chem. Neuroanat., May 1995, 8(4):283-305.
Matsui T, Hirano A (1978). An Atlas of the Human Brain for Computerized Tomography, Igako-Shoin.
Mattson SN, Riley EP, Sowell ER, Jernigan TL, Sobel DF, Jones KL (1996). A decrease in the size of the basal ganglia in children with fetal alcohol syndrome. Alcohol Clin Exp Res 1996 Sep;20(6):1088-93.
Mazziotta JC, Toga AW, Evans AC, Fox P, Lancaster J (1995) A Probabilistic Atlas of the Human Brain: Theory and Rationale for its Development, NeuroImage 2: 89-101.
Mega MS, Chen S, Thompson PM, Woods RP, Karaca TJ, Tiwari A, Vinters H, Small GW, Toga AW (1997) Mapping Pathology to Metabolism: Coregistration of Stained Whole Brain Sections to PET in Alzheimer's Disease, NeuroImage 5:147-153, Feb. 1997.
Mega MS, Dinov ID, Lee L, Woods RP, Thompson PM, Holmes CJ, Back CL, Collins DL, Evans AC, Toga AW (1998) Dissecting Neural Networks Underlying the Retrieval Deficit from the Amnestic Memory Disorder Using [99mTc]-HMPAO-SPECT, Proc. Amer. Behav. Neurol. Soc., Feb. 1998.
Mega MS, Thompson PM, Cummings JL, Back CL, Xu LQ, Zohoori S, Goldkorn A, Moussai J, Fairbanks L, Small GW, Toga AW (1998) *Sulcal Variability in the Alzheimer's Brain: Correlations with Cognition*, Neurology 50:145-151, January 1998.
Mega MS, Woods RP, Thompson PM, Dinov ID, Lee L, Aron J, Zoumalan CI, Cummings JL, Toga AW (1998). *Detecting Metabolic Patterns Associated with Minimal Cognitive Impairment using FDG-PET Analysis within a Probabilistic Brain Atlas based upon Continuum Mechanics*, Proc. Soc. Neurosci., 1998.
Meltzer CC, Frost JJ (1994). Partial Volume Correction in Emission-Computed Tomography: Focus on Alzheimer Disease, in: Functional Neuroimaging: Technical Foundations, Thatcher RW, Hallett M, Zeffiro T, John ER, Huerta M [eds.], Academic Press, 163-170.
Miller MI, Christensen GE, Amit Y, Grenander U (1993). Mathematical Textbook of Deformable Neuroanatomies, Proc. Nat. Acad. Sci. USA 90:11944-11948.
Minoshima S, Koeppe RA, Frey KA, Ishihara M, Kuhl DE (1994). Stereotactic PET Atlas of the Human Brain: Aid for Visual Interpretation of Functional Brain Images, J. Nucl. Med., 35:949-954.
Narayanan S, Fu L, Pioro E, De Stefano N, Collins DL, Francis GS, Antel JP, Matthews PM, Arnold DL (1997). Imaging of axonal damage in multiple sclerosis: spatial distribution of magnetic resonance imaging lesions. Ann Neurol 1997 Mar;41(3):385-91.
Narr KL, Cannestra AF, Thompson PM, Sharma T, Toga AW (1998). *Morphological Variability Maps of the Corpus Callosum and Fornix in Schizophrenia*, 4th Int. Conf. on Human Brain Mapping, NeuroImage 7(4):S506.
Narr KL, Thompson PM, Sharma T, Moussai J, Cannestra AF, Toga AW (1999). *Mapping Corpus Callosum Morphology in Schizophrenia*, Cerebral Cortex, [in press].
Nestor PG, Shenton ME, McCarley RW, Haimson J, Smith RS, O'Donnell B, Kimble M, Kikinis R, Jolesz FA: Neuropsychological correlates of MRI temporal lobe abnormalities in schizophrenia. Am J of Psychiatry 1993;150:12:1849-55.
Nowinski WL, Fang A, Nguyen BT, Raphel JK, Jagannathan L, Raghavan R, Bryan RN, Miller GA (1997). Multiple Brain Atlas Database and Atlas-Based Neuroimaging System, Comput. Aided Surg. 1997;2(1):42-66.
Ono M, Kubik S, Abernathey CD (1990) Atlas of the Cerebral Sulci. Stuttgart: Thieme.
Paus T, Tomaioulo F, Otaky N, MacDonald D, Petrides M, Atlas J, Morris R, Evans AC (1996). Human Cingulate and Paracingulate Sulci: Pattern, Variability, Asymmetry and Probabilistic Map, Cerebral Cortex 6:207-214.
Paus T, Zijdenbos A, Worsley K, Collins DL, Blumenthal J, Giedd JN, Rapoport JL, Evans AC (1999). Structural maturation of neural pathways in children and adolescents: in vivo study. Science 1999 Mar 19;283(5409):1908-11.
Payne BA, Toga AW (1990). Surface Mapping Brain Function on 3D Models, Comput. Graphics Appl. 10(5):33-41.

Petty RG, Barta PE, Pearlson GD, McGilchrist IK, Lewis RW, Tien AY, Pulver A, Vaughn DD, Casanova MF, Powers RE: Reversal of asymmetry of the planum temporale in schizophrenia. Am J of Psychiatry 1995;152:5:715-721.
Pfefferbaum A, Mathalon DH, Sullivan EV, Rawles JM, Zipursky RB, Lim KO (1994). A quantitative magnetic resonance imaging study of changes in brain morphology from infancy to late adulthood. Arch Neurol 1994 Sep;51(9):874-87.
Pitiot A, Thompson PM, Toga AW (1999). *Spatially and Temporally Adaptive Elastic Template Matching*, IEEE Transactions on Pattern Analysis and Machine Intelligence, 1999.
Piven J, Bailey J, Ranson BJ, Arndt S (1997) An MRI study of the corpus callosum in autism. American Journal of Psychiatry, 154(8): 1051-1056.
Pommert A, Schubert R, Riemer M, Schiemann T, Tiede U, Höhne KH (1994). Symbolic Modeling of Human Anatomy for Visualization and Simulation, IEEE Vis. Biomed. Comp. 2359:412-423.
Raz N, Torres IJ, Acker JD (1995). Age, gender, and hemispheric differences in human striatum: a
quantitative review and new data from in vivo MRI morphometry. Neurobiol Learn Mem 1995 Mar;63(2):133-42 .
Riley EP, Mattson SN, Sowell ER, Jernigan TL, Sobel DF, Jones KL (1995) Abnormalities of the corpus callosum in children prenatally exposed to alcohol. Alcoholism: Clinical and Experimental Research, 19(5): 1198-1202.
Roland PE, Zilles K (1994). Brain Atlases - A New Research Tool, Trends in Neurosciences 17(11):458-467.
Rizzo G, Gilardi MC, Prinster A, Grassi F, Scotti G, Cerutti S, Fazio F (1995). An Elastic Computerized Brain Atlas for the Analysis of Clinical PET/SPET Data, Eur. J. Nucl. Med. 22(11):1313-18.
Roebuck TM, Mattson SN, Riley EP (1998). A review of the neuroanatomical findings in children with fetal alcohol syndrome or prenatal exposure to alcohol. Alcohol Clin Exp Res 1998 Apr;22(2):339-44 .
Rosenberg DR, Keshavan MS, Dick EL, Bagwell WW, MacMaster FP, Birmaher B (1997). Corpus callosal morphology in treatment-naive pediatric obsessive compulsive disorder. Prog Neuropsychopharmacol Biol Psychiatry 1997 Nov;21(8):1269-83.
Royackkers N, Desvignes M, Revenu M (1996). Construction automatique d'un atlas adaptatif des sillons corticaux, ORASIS 96, Clermont-Ferrand, pp. 187-192, 1996.
Sandor SR, Leahy RM (1994). Matching Deformable Atlas Models to Pre-Processed Magnetic Resonance Brain Images, Proc. IEEE Conf. on Image Processing, 3:686-690.
Sandor SR, Leahy RM (1995). Towards Automated Labeling of the Cerebral Cortex using a Deformable Atlas, In: Bizais Y, Barillot C, Di Paola R [eds.], Info. Proc. in Med. Imag., June 1995, 127-138.
Schaltenbrand G, Bailey P (1959). Introduction to Stereotaxis with an Atlas of the Human Brain, New York, Stuttgart: Thieme.
Schaltenbrand G, Wahren W (1977). Atlas for Stereotaxy of the Human Brain, 2nd edn., Stuttgart: Thieme.
Schiemann T, Nuthmann J, Tiede U, Höhne KH (1996). Segmentation of the Visible Human for High-Quality Volume-Based Visualization, Vis. Biomed. Comp. 4:13-22.
Schiemann T, Höhne KH (1997). Definition of Volume Transformations for Volume Interaction, in: Duncan J, Gindi G [eds.], IPMI'97, Springer, Heidelberg.
Schmidt R (1992). Comparison of magnetic resonance imaging in Alzheimer's disease, vascular dementia and normal aging. Eur Neurol 1992;32(3):164-9.
Schormann T, Henn S, Zilles K (1996). *A New Approach to Fast Elastic Alignment with Applications to Human Brains*, Proc. Visualization in Biomed. Comp. 4:337-342.
Seitz RJ, Bohm C, Greitz T, Roland PE, Eriksson L, Blomqvist G, Rosenqvist G, Nordell B (1990). Accuracy and Precision of the Computerized Brain Atlas Programme for Localization and Quantification in Positron Emission Tomography, J. Cereb. Blood Flow. Metab. 10:443-457.
Semrud-Clikeman M, Filipek PA, Biederman J, Steingard R, Kennedy D, Renshaw P, Bekken K (1994) Attention-deficit hyperactivity disorder: magnetic resonance imaging morphometric analysis of the corpus callosum. J. American Academy of Child and Adolescent Psychiatry, 33(6):875-881.
Shenton ME, Kikinis R, Jolesz FA, Pollack SD, LeMay M, Wible CG, Hokama H, Martin J, Metcalf D, Coleman M, McCarley R: Abnormalities of the left temporal lobe and thought disorder in schizophrenia. New England J of Med 1992;327:9:604-612.
Siegel BV Jr, Shihabuddin L, Buchsbaum MS, Starr A, Haier RJ, Valladares Neto DC (1996). *Gender Differences in Cortical Glucose Metabolism in Alzheimer's Disease and Normal Aging*, J. Neuropsychiatry Clin. Neurosci. 8(2):211-214.
Smith GE (1907). A New Topographical Survey of the Human Cerebral Cortex, being an Account of the Distribution of the Anatomically Distinct Cortical Areas and their Relationship to the Cerebral Sulci, J. Anatomy 41:237-254.
Sobire G, Goutieres F, Tardieu M, Landrieu P, Aicardi J (1995). *Extensive Macrogyri or No Visible Gyri: Distinct Clinical, Electroencephalographic, and Genetic Features According to Different Imaging Patterns*, Neurology 45:1105-1111.
Sochen, N; Kimmel, R; Malladi, R (1998) A general framework for low level vision, IEEE Trans. on Image Processing, 1998 MAR, V7 N3:310-318.
Sowell ER, Jernigan TL, Mattson SN, Riley EP, Sobel DF, Jones KL (1996). Abnormal development of the cerebellar vermis in children prenatally exposed to alcohol: size reduction in lobules I-V. Alcohol Clin Exp Res 1996 Feb;20(1):31-4.
Spitzer V, Ackerman MJ, Scherzinger AL, Whitlock D (1996). The Visible Human Male: A Technical Report, J. Amer. Med. Informatics Assoc. 3(2):118-130. http://www.nlm.nih.gov/ extramural_research.dir/visible_human.html
Steinmetz H, Furst G, Freund H-J (1989) Cerebral Cortical Localization: Application and Validation of the Proportional Grid System in MR Imaging , J. of Comp. Assist. Tomography, 13(1):10-19.
Steinmetz H, Furst G, Freund H-J (1990) Variation of Perisylvian and Calcarine Anatomic Landmarks within Stereotaxic Proportional Coordinates, Amer. J. Neuroradiol., 11(6):1123-30.
Steinmetz H, Staiger JF, Schlaug G, Huang Y, Jancke L: Corpus callosum and brain volume in women and men. Neuroreport 1995;6:7:1002-4.

Stewart JE, Broaddus WC, Johnson JH (1996). Rebuilding the Visible Man, Vis. Biomed. Comp. 4:81-86.
St-Jean P, Sadikot AF, Collins L, Clonda D, Kasrai R, Evans AC, Peters TM (1998). Automated atlas integration and interactive three-dimensional visualization tools for planning and guidance in functional neurosurgery. IEEE Trans Med Imaging 1998 Oct;17(5):672-80 .
Strauss E, Kosaka B, Wada J (1983). *The Neurobiological Basis of Lateralized Cerebral Function. A Review*, Hum. Neurobiol. 2(3):115-127.
Subsol G, Roberts N, Doran M, Thirion JP, Whitehouse GH (1997). Automatic Analysis of Cerebral Atrophy, Magn. Reson. Imaging, 15(8):917-927.
Sundsten JW, Kastella JG, Conley DM (1991). Videodisc Animation of 3D Computer Reconstructions of the Human Brain, J. Biomed. Comm. 18:45-49.
Swayze VW, Johnson VP, Hanson JW, Piven J, Sato Y, Giedd JN, Mosnik D, Andreasen NC (1997) Magnetic resonance imaging of brain anomalies in fetal alcohol syndrome. Pediatrics, 99(2):232-40.
Talairach J, Szikla G (1967). Atlas d'Anatomie Stereotaxique du Telencephale: Etudes Anatomo-Radiologiques.Paris: Masson & Cie.
Talairach J, Tournoux P (1988). Co-planar Stereotaxic Atlas of the Human Brain, New York: Thieme.
Thirion J-P (1995). Fast Non-Rigid Matching of Medical Images, INRIA Internal Report 2547, Projet Epidaure, INRIA, France.
Thirion J-P, Calmon G (1997) *Deformation Analysis to Detect and Quantify Active Lesions in 3D Medical Image Sequences*, INRIA Technical Report 3101, Feb. 1997.
Thirion J-P, Prima S, Subsol S (1998). *Statistical Analysis of Dissymmetry in Volumetric Medical Images*, Medical Image Analysis [in press].
Thompson PM, Schwartz C, Toga AW (1996a). High-Resolution Random Mesh Algorithms for Creating a Probabilistic 3D Surface Atlas of the Human Brain, NeuroImage 3:19-34.
Thompson PM, Schwartz C, Lin RT, Khan AA, Toga AW (1996b). 3D Statistical Analysis of Sulcal Variability in the Human Brain, Journal of Neuroscience, Jul. 1996, 16(13):4261-4274.
Thompson PM, Toga AW (1996c). A Surface-Based Technique for Warping 3-Dimensional Images of the Brain, IEEE Transactions on Medical Imaging, Aug. 1996, 15(4):1-16.
Thompson PM, MacDonald D, Mega MS, Holmes CJ, Evans AC, Toga AW (1997a). Detection and Mapping of Abnormal Brain Structure with a Probabilistic Atlas of Cortical Surfaces, J. Comp. Assist. Tomogr. 21(4):567-581, Jul.-Aug. 1997.
Thompson PM, Toga AW (1997b) Detection, Visualization and Animation of Abnormal Anatomic Structure with a Deformable Probabilistic Brain Atlas based on Random Vector Field Transformations, Medical Image Analysis 1(4):271-294.
Thompson PM, Moussai J, Khan AA, Zohoori S, Goldkorn A, Mega MS, Small GW, Cummings JL, Toga AW (1998). Cortical Variability and Asymmetry in Normal Aging and Alzheimer's Disease, Cerebral Cortex 8(6):492-509, Sept.1998.
Thompson PM, Toga AW (1998) Anatomically-Driven Strategies for High-Dimensional Brain Image Warping and Pathology Detection, in: Brain Warping, (Toga AW, ed.), Academic Press, 311-336, Nov. 1998.
Thompson PM, Giedd JN, Blanton RE, Lindshield C, Woods RP, MacDonald D, Evans AC, Toga AW (1998). *Growth Patterns in the Developing Human Brain Detected Using Continuum-Mechanical Tensor Maps and Serial MRI*, 5th Int. Conf. on Human Brain Mapping, Montreal, Canada.
Thompson PM, Narr KL, Blanton RE, Toga AW (1999). *Mapping Structural Alterations of the Corpus Callosum during Brain Development and Degeneration*, in: Iacoboni M, Zaidel E [eds.], *The Corpus Callosum*, Kluwer Academic Press [in press].
Thompson PM, Toga AW (1998b). *Mathematical/Computational Strategies for Creating a Probabilistic Atlas of the Human Brain, Workshop on Statistics of Brain Mapping*, Centre de Recherches Mathématiques, McGill University, Canada, June 13-14 1998.
Thompson PM, Woods RP, Mega MS, Toga AW (1999). Mathematical/Computational Challenges in Creating Population-Based Brain Atlases, Human Brain Mapping 8(2), September 1999.
Thompson PM, Toga AW (1999). *Elastic Image Registration and Pathology Detection*, Book Chapter in: Bankman I, Rangayyan R, Evans AC, Woods RP, Fishman E, Huang HK [eds.], Handbook of Medical Image Processing, Academic Press, 1999.
Thurfjell L, Bohm C, Greitz T, Eriksson L (1993). Transformations and Algorithms in a Computerized Brain Atlas, IEEE Trans. Nucl. Sci., 40(4), pt. 1:1167-91.
Tiede U, Bomans M, Höhne KH, Pommert A, Riemer M, Schiemann T, Schubert R, Lierse W (1993). A Computerized 3D Atlas of the Human Skull and Brain, Am. J. Neuroradiol. 14:551-559.
Toga AW, Ambach K, Quinn B, Hutchin M, Burton JS (1994). Postmortem Anatomy from Cryosectioned Whole Human Brain, J. Neurosci. Methods, Oct. 1994, 54(2):239-252.
Toga AW (1994). Visualization and Warping of Multimodality Brain Imagery, in: Functional Neuroimaging: Technical Foundations, Thatcher RW, Hallett M, Zeffiro T, John ER, Huerta M [eds.], 171-180.
Toga AW, Mazziotta JC (1996). Brain Mapping: The Methods, Academic Press.
Toga AW, Thompson PM, Payne BA (1996). Modeling Morphometric Changes of the Brain during Development, chapter in: Developmental Neuroimaging: Mapping the Development of Brain and Behavior, Thatcher RW, Lyon GR, Rumsey J, Krasnegor N, eds., Academic Press.
Toga AW, Thompson PM (1997) Measuring, Mapping, and Modeling Brain Structure and Function, SPIE Medical Imaging Symposium, Feb. 1997, Newport Beach, CA, USA; SPIE Lecture Notes Volume 3033.
Toga AW (1998). *Brain Warping*, Academic Press.
Toga AW, Goldkorn A, Ambach K, Chao K, Quinn BC, Yao P (1997). Postmortem cryosectioning as an anatomic reference for human brain mapping. Comput Med Imaging Graph 1997 Mar-Apr;21(2):131-41
Toga AW, Thompson PM (1998). *An Introduction to Brain Warping*, in: *Brain Warping*, (Toga AW, ed.), Academic Press.
Toga AW, Thompson PM (1998). *Multimodal Brain Atlases*, Chapter in: *Medical Image Databases*, Wong STC [ed.], Kluwer Academic Press, pp.53-88.
Toga AW, Thompson PM (1999). *An Introduction to Maps and Atlases of the Brain*, Book Chapter in: *Brain Mapping: The Applications*, Toga AW, Mazziotta JC [eds.], Academic Press, 1999.

Toga AW, Thompson PM (1999). *Brain Atlases and Image Registration*, Book Chapter in: Bankman I, Rangayyan R, Evans AC, Woods RP, Fishman E, Huang HK [eds.], Handbook of Medical Image Processing, Academic Press [to appear, 1999].
Vaillant M, Davatzikos C (1999), Hierarchical Matching of Cortical Features for Deformable Brain Image Registration, Proc. Information Processing in Medical Imaging, Budapest, June 1999.
Van Buren JM, Maccubin D (1962). An Outline Atlas of Human Basal Ganglia and Estimation of Anatomic Variants, J. Neurosurg. 19:811-839.
Van Buren JM, Borke RC (1972). Variations and Connections of the Human Thalamus, Vols. 1 & 2. New York: Springer.
Van Essen DC, Drury HA, Joshi SC, Miller MI (1997). *Comparisons between Human and Macaque using Shape-Based Deformation Algorithms Applied to Cortical Flat Maps*, 3rd Int. Conference on Functional Mapping of the Human Brain, Copenhagen, May 19-23 1997, NeuroImage 5(4):S41.
Viola PA, Wells WM (1995). Alignment by Maximization of Mutual Information, 5th IEEE Int. Conf. on Computer Vision, 16-23, Cambridge, MA.
Waddington JL: Neurodynamics of abnormalities in cerebral metabolism and structure in schizophrenia. Schizophrenia Bulletin 1993;19:55-8.
Wang PP, Doherty S, Hesselink JR, Bellugi U (1992). Callosal morphology concurs with neurobehavioral and neuropathological findings in two neurodevelopmental disorders. Arch Neurol 1992 Apr;49(4):407-11.
Warfield S, Dengler J, Zaers J, Guttmann CRG, Wells WM, Ettinger GJ, Hiller J, Kikinis R (1995). Automatic Identification of Gray Matter Structures form MRI to Improve the Segmentation of White Matter Lesions, Proc. Med. Robotics & Comp. Assist. Surg (MRCAS), Nov. 4-7 1995, 55-62.
Warfield S, Robatino A, Dengler J, Jolesz F, Kikinis R (1998) Nonlinear Registration and Template Driven Segmentation, In: Brain Warping. Ed. Arthur W. Toga, AcademicPress, Ch.4:67-84, 1998.
Watson JDG, Myers R, Frackowiak RSJ, Hajnal JV, Woods RP, Mazziotta JC, Shipp S, Zeki S (1993). Area V5 of the Human Brain: Evidence form a Combined Study using Positron Emission Tomography and Magnetic Resonance Imaging, Cereb. Cortex 3:79-94.
Wells WM, Viola P, Atsumi H, Nakajima S, Kikinis R (1997). Multi-Modal Volume Registration by Maximization of Mutual Information, Medical Image Analysis 1(1):35-51.
West MJ, Coleman PD, Flood DG, Troncoso JC (1994). *Differences in the Pattern of Hippocampal Neuronal Loss in Normal Aging and Alzheimer's Disease*, Lancet 344:769-772.
Whitehouse PJ, Price DL, Clark AW, Coyle JT, DeLong MR (1981). *Alzheimer's Disease: Evidence for Selective Loss of Cholinergic Neurons in the Nucleus Basalis*, Ann. Neurol. 10:122-126.
Witelson SF: Hand and sex differences in the isthmus and genu of the human corpus callosum. A postmortem morphological study. Brain 1989;112:799-835.
Woods RP, Cherry SR, Mazziotta JC (1992). Rapid Automated Algorithm for Aligning and Reslicing PET Images. Journal of Computer Assisted Tomography 16:620-633.
Woods RP, Mazziotta JC, Cherry SR (1993). MRI-PET Registration with Automated Algorithm, Journal of Computer Assisted Tomography 17:536-546.
Woods RP (1996). Modeling for Intergroup Comparisons of Imaging Data, NeuroImage 4(3):84-94.
Woods RP, Grafton ST, Watson JDG, Sicotte NL, Mazziotta JC. *Automated image registration: II. Intersubject validation of linear and nonlinear models.* J. Computer Assisted Tomography 1998;22: (in press).
Worsley KJ (1994a). Quadratic Tests for Local Changes in Random Fields with Applications to Medical Images, Technical Report, Department of Mathematics and Statistics, McGill University, 94-08.
Worsley KJ (1994b). Local Maxima and the Expected Euler Characteristic of Excursion Sets of Chi-squared, F and t Fields, Advances in Applied Probability, 26:13-42.
Zhou Y, Thompson PM, Toga AW (1999). *Automatic Extraction and Parametric Representations of Cortical Sulci*, Computer Graphics and Applications 19(3):49-55, May 1999.
Zijdenbos AP, Dawant BM (1994). Brain Segmentation and White Matter Lesion Detection in MR Images, Crit. Rev. Biomed. Eng. 22(5-6):401-465.
Zoumalan CI, Mega MS, Thompson PM, Fuh JL, Lindshield C, Toga AW (1999). *Mapping 3D Patterns of Cortical Variability in Normal Aging and Alzheimer's Disease,* Annual Conference of the American Academy of Neurology.

…….

Figure Legends

Fig. 1. *Elements of a Disease-Specific Atlas.* This schematic shows the types of maps and models contained in a disease-specific brain atlas. In the main text, we explain how these maps are created, and review their applications. Examples are shown from an atlas that represents an Alzheimer's Disease population. To construct the atlas, databases of structural imaging data are used to develop detailed models of cortical structure and anatomic subsystems. These models are statistically combined to create group average models that can be compared with a normal database. Patterns of variability, asymmetry, and disease-specific differences are also computed from the anatomic data. Specialized techniques create a well-resolved average image template for the patient population (Continuum-Mechanical Template, *center right*). This template provides a coordinate framework to link *in vivo* metabolic and functional data with fine-scale anatomy and biochemistry. In recent studies (Mega et al., 1997), histologic maps of *post mortem* neurofibrillary tangle (NFT) staining

density were correlated with *in vivo* metabolism. 3D FDG-PET data, obtained 8 hours before death, was compared with whole-brain cryosections acquired immediately *post mortem* and stained for NFTs by the Gallyas method. Using the algorithm of (Thompson and Toga, 1996; *warped image*), distorted tissue sections were elastically warped back to their configuration in the cryosection blockface (*top row*). A further 3D registration projected the data into pre-mortem MR and co-registered PET data (*top right*).

Fig. 2. *Elastic Registration of Brain Maps and Molecular Assays*. *Post mortem* tissue sections, from patients with Alzheimer's Disease, are gridded (*left*) to produce tissue elements for biochemical assays. These assays provide detailed quantitative measures of the major hallmarks of AD, including beta-amyloid and synaptophysin density. To pool this data in a common coordinate space, tissue elements are elastically warped back into their original configuration in the cryosection blockface (middle panel). Image data acquired from the same patient in vivo can then be correlated with regional biochemistry (Mega et al., 1997). When tissue sections are warped to the blockface, continuum-mechanical models are used to make the deformations reflect how real physical tissues deform. The complexity of the required deformation vector field in a small tissue region (*magnified vector map, right*) demonstrates that very flexible, high-dimensional transformations are essential (Thompson and Toga, 1996; Schormann et al., 1996; Christensen et al., 1996). These deformation vector fields project histologic and biochemical data back into their *in vivo* configuration, populating a growing Alzheimer's Disease atlas with maps of molecular content and histology.

Fig. 3. *Models of Deep Sulcal and Ventricular Surfaces can Measure Anatomic Differences across Subjects*. Parametric surface models of deep anatomic structures can guide the mapping of one brain to another (data from Thompson and Toga, 1996). This mapping measures anatomic differences between two subjects. Deep sulcal surfaces include: the anterior and posterior calcarine (CALCa/p), cingulate (CING), parieto-occipital (PAOC) and callosal (CALL) sulci and Sylvian fissure (SYLV). Also shown are the superior and inferior surfaces of the rostral horn (VTSs/i) and inferior horn (VTIs/i) of the right lateral ventricle. Ventricles and deep sulci are represented by connected systems of rectangularly-parameterized surface meshes, while the external surface has a spherical parameterization (Section 8). Connections are introduced between elementary mesh surfaces at known tissue-type and cytoarchitectural field boundaries, and at complex anatomical junctions (such as the PAOC/CALCa/CALCp junction shown here). Color-coded profiles show the magnitude of the 3D deformation maps warping these surface components (in the right hemisphere of a 3D T_1-weighted SPGR MRI scan of an Alzheimer's patient) onto their counterparts in an age-matched normal subject.

Fig. 4. *Continuum-Mechanical Warping*. (a) The complex transformation required to reconfigure one brain into the shape of another can be determined using continuum-mechanical models, which describe how real physical materials deform. In this illustration, two line elements embedded in a linearly elastic 3D block (*lower left*) are slightly perturbed (*arrows*). The goal is to find how the rest of the material deforms in response to this displacement. The Cauchy-Navier equations (shown in discrete form, *top*) are solved to determine the values of the displacement field vectors, **u(x),** throughout the 3D volume. (b) *Lamé Elasticity Coefficients*. Different choices of elasticity coefficients, λ and μ, in the Cauchy-Navier equations (shown in continuous form, *top*) result in different deformations, even if the applied internal displacements are the same. In histologic applications where an elastic tissue deformation is estimated, values of the elasticity coefficients can be chosen which limit the amount of curl (*lower right*) in the deformation field. Stiffer material models (*top left*) may better reflect the deformational behavior of tissue during histologic staining procedures. *Note*: To emphasize differences, the displacement vector fields shown in this figure have been multiplied by a factor of 10. The Cauchy-Navier equations, derived using an assumption of small displacements, are valid only when the magnitude of the deformation field is small.

Fig. 5. *Mesh Construction and Averaging*. The derivation of a standard surface representation for each structure makes it easier to compare anatomical models from multiple subjects. An algorithm converts a set of digitized points on an anatomical structure boundary (e.g., deep sulci, *top left*) into a parametric grid of uniformly spaced points in a regular rectangular mesh stretched over the surface (Thompson et al., 1996). By averaging nodes with the same grid coordinates across subject (bottom left), an average surface can be produced for the group. However, information on each subject's individual differences is stored as a vector-valued displacement map (*bottom right*). This map indicates how that subject deviates locally from the average anatomy. These maps can be stored to measure variability and detect abnormalities in different anatomic systems.

Fig. 6. *Partitioning the Ventricles into 3D Surface Elements.* A model of the lateral ventricles is shown, in the context of a coronal anatomic image and a smoothed cortical surface mesh. The ventricles are partitioned into 14 connected surface elements, whose junctions reflect tissue type boundaries at the ventricular surface. For example, a combination of caudate, thalamic, and septal tissues (as well as callosal fibers) surround the superior ventricular horn, and each exhibits different patterns of variation and asymmetry (Fig. 8). To ensure that these parameters are not confounded, each ventricular element is modeled separately.

Fig. 7. *A Deformable Cryosection Atlas Measures Anatomic Differences.* Structure boundaries from a patient with Alzheimer's disease (*top left*) are overlaid on a cryosection atlas (*top right*), which has been registered to it using a simple linear transformation. A surface-based image warping algorithm is then applied to drive the atlas into the configuration of the patient's anatomy (*bottom left*). Histologic and neurochemical maps, accessible only post mortem, can be transferred onto the living subject's scan (Mega et al., 1997). The amount of deformation required is displayed as a tensor map (only 2 components of the fully 3D transformation are shown). Tensor maps, and derived vector or scalar fields, can be analyzed in a statistical setting to examine anatomic variation, detect pathology, or track structural changes over time.

Fig. 8. *Population-Based Maps of 3D Structural Variation and Asymmetry*. Statistics of 3D deformation maps help define confidence limits on normal anatomic variation. 3D maps of anatomic variability and asymmetry are shown for 10 subjects with Alzheimer's Disease (AD; age: 71.9±10.9 yrs.), and 10 normal elderly subjects matched for age (72.9±5.6 yrs.), gender, handedness and educational level (Thompson et al., 1998). Normal Sylvian fissure asymmetries (right higher than left; $p<0.0005$) were significantly greater in AD than in controls ($p<0.0002$; *top panels*). In the 3D variability maps derived for each group (*lower panels*), the color encodes the root mean square magnitude of the displacement vectors that map surfaces from each of the ten patients' brains onto the average. 3D cortical variability (*lower right panel*) increased in AD from 2-4 mm at the *corpus callosum* to a peak standard deviation of 19.6 mm at the posterior left Sylvian fissure.

Fig. 9. *Population-Based Maps of Ventricular Anatomy in Normal Aging and Alzheimer's Disease*. 3D parametric surface meshes (Thompson et al., 1996) were used to model the 14 ventricular elements, shown in Fig. 6, in 3D MRI scans of 10 Alzheimer's patients (age: 71.9±10.9 yrs.) and 10 matched controls (72.9±5.6 yrs.; Thompson et al., 1998). 3D meshes representing each surface element were averaged by hemisphere in each group. (*top*:) The color map shows a 3D r.m.s. measure of group anatomic variability pointwise on an average surface representation for each group, in Talairach stereotaxic space. Oblique side views reveal enlarged occipital horns in the Alzheimer's patients, and high stereotaxic variability in both groups. (*lower panels*:) A top view of these averaged surface meshes reveals localized asymmetry, variability, and displacement within and between groups. Asymmetries at the ventricles and Sylvian fissure emerge only after averaging of anatomical maps in large groups of subjects. These patterns can be encoded probabilistically to detect structural anomalies in individual patients or groups (Thompson et al., 1997).

Fig. 10. *Corpus Callosum in Alzheimer's Disease*. Midsagittal *corpus callosum* boundaries were averaged from patients with Alzheimer's Disease and from elderly controls matched for age, educational level, gender and handedness. The average representations show a focal shape inflection in the Alzheimer's patients relative to normal elderly subjects of the same age. A statistically significant tissue loss is also found at the isthmus (2^{nd} sector, when the structure is partitioned into fifths). The isthmus connects regions of temporo-parietal cortex that exhibit early neuronal loss and perfusion deficits in AD (Thompson et al., 1998).

Fig. 11. *Corpus Callosum in Schizophrenia*. [Data from Narr et al., 1999]. Midsagittal *corpus callosum* boundaries were averaged from 25 patients with chronic schizophrenia (DSM-III-R criteria; 15 males, 10 females; age: 31.1 +/- 5.6 yrs.) and from 28 control subjects matched for age (30.5 +/- 8.7 yrs.), gender (15 males, 13 females) and handedness (1 left-handed subject per group). Profiles of anatomic variability around the group averages are also shown (*in color*) as an r.m.s. deviation from the mean. Anatomical averaging reveals a pronounced and significant bowing effect in the schizophrenic patients relative to normal controls. Male patients show a significant increase in curvature for superior and inferior callosal boundaries ($p < 0.001$), with a highly significant Sex by Diagnosis interaction ($p < 0.004$). The sample was stratified by Sex and Diagnosis and separate group averages show that the disease induces less bowing in females (*panel 1*) than in males (*panel 2*). While gender differences are not apparent in controls (*panel 3*), a clear gender difference is seen in the schizophrenic patients (*panel 4*). Abnormalities localized in a disease-specific atlas can therefore be analyzed to reveal interactions between disease

and demographic parameters.

Fig. 12. *Distortions in Brain Architecture induced by Tumor Tissue: Probability Maps for Ventral Callosum and Major Sulci*. Color-coded probability maps, (b), quantify the impact of two focal metastatic tumors (*illustrated in red;* see cryosection blockface, (a)) on the ventral callosal boundary, as well as the parieto-occipital and anterior and posterior calcarine sulci in both brain hemispheres.

Fig. 13. *Probabilistic Labeling of Structures in Image Databases.* An atlas storing information on anatomic variability is used to guide an algorithm in finding the *corpus callosum* boundary (*panel 9*) in each image in an anatomic database (N=104; Pitiot et al., 1999). The output of an edge detector (*panel 2*) is run through a connectivity filter that suppresses the smallest connected sets of edge pixels. The filtered edge image is then diffused over time (*panels 4-6*) and a deformable curve (*panel 7*) is adapted to optimize a matching measure (*panel 10*). This measure penalizes curve shapes that are (1) too bent or stretched, that (2) fail to overlap the diffused edge image, or that (3) are unlikely based on a statistical distribution of normal corpus callosum shapes. Given an image database, algorithm parameters (such as the size of the connectivity filter; *panel 11*) can be tuned based on their overall performance on an image database. Their optimal values differ depending on how noisy the images are. Boundaries can then be averaged from patients with dementia or schizophrenia to detect anomalies. Using separate sets of training and test images, these algorithms can both *invoke* and *generate* information on structural variation and pathology.

Fig. 14. *Maps of the Human Cerebral Cortex: Flat Maps, Spherical Maps, and Tensor Maps.* Extreme variations in cortical anatomy (*3D Models; top left*) present challenges in brain mapping, because of the need to compare cortically-derived brain maps from many subjects. Comparisons of cortical geometry can be based on the warped mapping of one subject's cortex onto another (*top right*; Thompson et al., 1997). These warps can also transfer functional maps from one subject to another, or onto a common template for comparison. Current approaches for deforming one cortex into the shape of another, typically simplify the problem by first representing cortical features on a 2D plane, sphere or ellipsoid, where the matching procedure (i.e. finding $\mathbf{u}(\mathbf{r}_2)$, above) is subsequently performed (Thompson and Toga, 1996, Davatzikos et al., 1996; Drury et al., 1996; Van Essen et al., 1997; Bakircioglu et al., 1999; Vaillant and Davatzikos, 1999). In one approach (Thompson et al., 1997), active surface extraction of the cortex provides a continuous inverse mapping from the cortex of each subject to the spherical template used to extract it. These inverse maps are applied to connected networks of curved sulci in each subject. This transforms the problem into one of computing an angular flow vector field $\mathbf{u}(\mathbf{r}_2)$, in spherical coordinates, which drives the network elements into register on the sphere (*middle panel*; Thompson and Toga, 1996). The full mapping (*top right*) can be recovered in 3D space as a displacement vector field which drives cortical points and regions in one brain into register with their counterparts in the other brain. *Tensor Maps (middle and lower left):* Although these simple 2-parameter surfaces can serve as proxies for the cortex, different amounts of local dilation and contraction (encoded in the metric tensor if the mapping, $g_{jk}(\mathbf{r})$) are required to transform the cortex into a simpler 2-parameter surface. These variations complicate the direct application of 2D regularization equations for matching their features. A covariant tensor approach is introduced in (Thompson and Toga, 1998a,b; *see red box*) to address this difficulty. The regularization operator L is replaced by its covariant form L*, in which correction terms (Christoffel symbols, Γ^{i}_{jk}) compensate for fluctuations in the metric tensor of the flattening procedure. A covariant tensor approach (Thompson and Toga, 1998a,b) allows either flat or spherical maps to support cross-subject comparisons and registrations of cortical data by eliminating the confounding effects of metric distortions which necessarily occur in the flattening procedure.

Fig. 15. *Gyral Pattern Matching*. Gyral patterns can be matched in a group of subjects to create average cortical surfaces. (a) shows a cortical flat map for the left hemisphere of one subject, with the average cortical pattern for the group overlaid (*colored lines*). (b) shows the result of warping the individual's sulcal pattern into the average configuration for the group, using the covariant field equations (Section 8). The individual cortex (a) is reconfigured (b) to match the average set of cortical curves. The 3D cortical regions that map to these average locations are then recovered in each individual subject, as follows. A color code (c) representing 3D cortical point locations (e) in this subject is convected along with the flow that drives the sulcal pattern into the average configuration for the group (d). Once this is done in all subjects, points on each individual's cortex are recovered (f) that have the same relative location to the primary folding pattern in all subjects. Averaging of these corresponding points results in a crisp average cortex (Fig. 15). These transformation fields are stored and used to measure regional variability.

Fig. 16. *Average Cortex in Alzheimer's Disease*. The average cortical surface for a group of subjects (*N*=9, Alzheimer's patents) is shown as a graphically rendered surface model. If sulcal position vectors are averaged without aligning the intervening gyral patterns (*top*), sulcal features are not reinforced across subjects, and a smooth average cortex is produced. By matching gyral patterns across subjects before averaging, a crisper average cortex is produced (*bottom row*). Sulcal features that consistently occur across all subjects appear in their average geometric configuration.

Fig. 17. *Matching an Individual's Cortex to the Average Cortex.* 3D variability patterns across the cortex are measured by driving individual cortical patterns into local correspondence with the average cortical model. (a) shows how the anatomy of one subject (*brown surface mesh*) deviates from the average cortex (*white*), after affine alignment of the individual data. (b) shows the deformation vector field required to reconfigure the gyral pattern of the subject into the exact configuration of the average cortex. The transformation is shown as a flow field that takes the individual's anatomy onto the right hemisphere of the average cortex (*blue surface mesh*). The largest amount of deformation is required in the temporal and parietal cortex (*pink colors, large deformation*). Details of the 3D vector deformation field ((b), *inset*) show the local complexity of the mapping.

Fig. 18. *3D Cortical Variability in Talairach Stereotaxic Space*. (a) The profile of variability across the cortex is shown (*N*=26 Alzheimer's patients), after differences in brain orientation and size are removed by transforming individual data into Talairach stereotaxic space. The following views are shown: oblique frontal, frontal, right, left, top, bottom. Extreme variability in posterior perisylvian zones and superior frontal association cortex (16-18 mm; *red colors*) contrasts sharply with the comparative invariance of primary sensory, motor, and orbitofrontal cortex (2-5 mm, *blue colors*).

Fig. 19. *Tensor Maps Reveal Directional Biases of Cortical Variation.* Tensor maps can be used to visualize these complex patterns of gyral pattern variation at the cortex. The maps are based on a group of 20 elderly normal subjects. Color distinguishes regions of high variability (*pink colors*) from areas of low variability (*blue*). Rectangular glyphs indicate the principal directions of variation - they are most elongated along directions where there is greatest anatomic variation across subjects. Each glyph represents the covariance tensor of the vector fields that map individual subjects onto their group average anatomic representation. The resulting information can be leveraged to distinguish normal from abnormal anatomical variants using random field algorithms, and can define statistical distributions for feature labeling at the cortex (*cf.* Le Goualher et al., 1999; Vaillant and Davatzikos, 1999).

Fig. 20. *Confidence Limits on Normal Anatomic Variation: Tensor Field Representation*. Again, two tensor maps reveal the preferred directions of cortical variation, after sulcal pattern correspondences are taken into account. Variability is greatest in temporo-parietal cortex. If cortical variations are modeled as vector field displacements of an average cortical model, ellipsoids of constant probability density can be computed for positions of cortical regions (relative to the average cortex). These ellipsoids are shown, colored by the determinant of the covariance tensor. Fields of tumbling ellipses have also been used to visualize multi-directional parameters in diffusion imaging data, and offer a means to represent cortical variability for anomaly detection and Bayesian image labeling.

Fig. 21. *Anatomical Variability of the Cerebral Cortex. (N=15, Schizophrenia Patients, and N=15 Matched Controls; all males).* [Data from Narr et al. (1999)]. 3D maps of variability are shown on average surface representations of the cortex derived from a schizophrenia (*left*) and normal control population (*right*). In frontal association cortex (*red colors*), schizophrenic patients exhibit greater individual variations in gyral patterns. Contrary to several recent research reports, the marked brain asymmetry in temporo-parietal cortex is clearly apparent in the schizophrenic patients as well as in controls. Again, variability is calculated based on 3D displacement maps, which locally encode the amount of deformation required to drive each subject's gyral pattern into exact correspondence with the average cortex for the group (see Section 8).

Fig. 22. *Mapping a Patient into the Group Average Configuration.* Instead of matching just the cortex, this figure shows the complex transformation required to match 84 different surface models in a given patient, after affine alignment, into the configuration of an average surface set derived for the group (see Thompson et al., 1999, for details). The effects of several anatomic surfaces driving the transformation are indicated, including the cingulate sulcus (CING), hippocampal surface (HPCP), superior ventricular horn (VTS), parieto-occipital sulcus, and the anterior calcarine fissure (CALCa). This surface-

based vector field is extended to a full volumetric transformation field (0.1 billion degrees of freedom) which reconfigures the anatomy of the patient into correspondence with the average configuration for the group. Storage of these mappings allows quantification of local anatomic variability.

Fig. 23. *Average Brain Templates*. Axial, sagittal and coronal images are shown from a variety of population-based brain image templates. For comparison purposes, (a) shows a widely-used average intensity dataset (ICBM305) based on 305 young normal subjects, created by the *International Consortium for Brain Mapping* (Evans et al., 1994); by contrast, templates (b) and (c) are average brain templates created from high-resolution 3D MRI scans of Alzheimer's Disease patients. (b) *Affine Brain Template*, constructed by averaging normalized MR intensities on a voxel-by-voxel basis data after automated affine registration; (b) *Continuum-Mechanical Brain Template*, based on intensity averaging after continuum-mechanical transformation. By using spatial transformations of increasing complexity, each patient's anatomy can increasingly be reconfigured into the average anatomical configuration for the group. After intensity correction and normalization, the reconfigured scans are then averaged on a pixel-by-pixel basis to produce a group image template with the average geometry and average image intensity for the group. Anatomical features are highly resolved, even at the cortex (c). Transformations of extremely high spatial dimension are required to match cortical features with sufficient accuracy to resolve them after scans are averaged together.

Fig. 24. *Tensor Maps of Growth*. (*top panel*:) A complex pattern of growth is detected in the *corpus callosum* of a young normal male subject in the 4-year period from 7 to 11 years of age. Vector field operators emphasize patterns of contractions and dilations, emphasizing their regional character. The color code shows values of the local Jacobian of the warping field, which indicates local volume loss or gain. The effects of the transformation are shown on a regular grid ruled over the reference anatomy and passively carried along in the transformation that matches it with the later anatomy. Despite minimal changes in overall cerebral volume, callosal growth is dramatic, with peak values throughout the isthmus and posterior midbody (*top panel*). Rapid heterogeneous growth, with a similar topographic pattern, is also observed in two young normal females (*next two panels*), during a one-year period from the age of 6 to 7, and during a 4-year period spanning puberty, from 9 to 13 years of age. The final panel shows growth mapped in a male subject across a period of 4 years from 11 to 15 years of age. Growth rates have clearly attenuated, but have a similar pattern to that of the younger subjects.

Fig. 25. *3D Patterns of Deep Nuclear Tissue Loss*. In the 4-year period from 7 to 11 years of age, a young normal male subject displays a local 50% tissue *loss* at the caudate head, as well as a 20-30% growth of the internal capsule and a 5-10% dilation of the superior ventricular horn (Thompson et al., 1999). Graphical visualizations of growth rates indicate the regional complexity of the growth processes between the two scans.

……

Table 1. ***Morphometric Abnormalities in Disease*****.** Although not an exhaustive list, this table summarizes the anatomic alterations found in major neurological diseases, as well as confounding differences due to demographic factors. Most recent studies have used large archives of volumetric (3D) MRI scans to detect structural alterations in disease. Disease-specific atlases offer a computational framework to combine digital structure models from large clinical subpopulations, localizing group differences. Once models are in a conveniently parameterized format, they can be statistically combined to reveal group-specific features not observable in individual data. Patterns of average asymmetry and variation also emerge. Complementary to the more traditional volumetric descriptors, computational models and images can be combined to build probabilistic atlases that localize regional abnormalities.

Alzheimer's Disease Sulcal and ventricular enlargement; gross cerebral atrophy, starting in temporal and parietal areas (Kido et al., 1989; Erkinjuntti et al., 1993; Killiany et al., 1993), entorhinal cortex (Arnold et al., 1991; Braak and Braak, 1991), the basal nucleus of Meynert (Whitehouse et al., 1991), amygdala (Cuénod et al., 1993), and hippocampus (West et al., 1994); caudate, lenticular and thalamic atrophy also reported (Jernigan et al., 1991).

Schizophrenia Enlarged lateral and 3rd ventricles (median 40% increase; Lawrie and Abukmeil, 1998); reduced brain volume (averaging 3%) with disproportionate temporal lobe reductions and gray matter deficits (including hippocampus; Lawrie and Abukmeil, 1998; Csernansky et al., 1998; Joshi et al., 1998); shape difference (Casanova et al., 1990; DeQuardo et al., 1996; Bookstein, 1997) or increased

bowing of corpus callosum, stronger in male patients (Narr et al., 1999); thalamic and midline anomalies (Andreasen et al., 1994, 1995); striatal enlargement secondary to antipsychotic medication (Chakos et al., 1994; Harrison, 1999); loss or reversal of cortical pattern asymmetry (Falkai et al., 1992; Shenton et al., 1992; Bilder et al., 1994).

Epilepsy Abnormal hippocampal morphology, including unilateral or bilateral volume loss, in patients with temporal lobe epilepsy (TLE; Jack, 1994); left temporal lobe may atrophy faster in left unilateral TLE than right temporal lobe in right unilateral TLE.

Autism Regional cerebral enlargement in posterior, temporal, and occipital but not frontal cortices; enlarged total cerebellar volume (Piven et al., 1997); controversy over localized hypoplasia at the cerebellar vermis, lobules VI and VII; possible hypoplastic and hyperplastic subgroups (Courchesne et al., 1994; Filipek, 1995).

ADHD 4.7% smaller total cerebral volume ($p < 0.02$) and smaller cerebellum, with significant loss of normal right > left caudate asymmetry and reversal of lateral ventricular asymmetry (Castellanos et al., 1996). Reduced area of the callosal splenium (Semrud-Clikeman et al., 1994; Lyoo et al., 1996), genu (Hynd et al., 1991) and rostrum (Giedd et al., 1994; Baumgardner et al., 1996).

Down's Syndrome Reduced frontal lobe volume (Jernigan et al., 1993) and reduced anterior callosal area (Wang et al., 1992); reduced volume in cerebellar hemispheres and hippocampus (Raz et al., 1995).

Fetal Alcohol Syndrome Striatal, callosal and cerebellar abnormalities (Roebuck et al., 1998). Complete or partial agenesis of the corpus callosum (Riley et al., 1995; Johnson et al., 1996); midline anomalies (callosal hypoplasia, *cavum septi pellucidi* and *cavum vergae*) associated with increased number of facial anomalies (Swayze et al., 1997). Reduced size of basal ganglia (Mattson et al., 1996) and vermian lobules I-V (Sowell et al., 1996).

Obsessive Compulsive Disorder (OCD) Smaller striatal volumes in pediatric OCD, inversely correlated with symptom severity (Rosenberg et al., 1997; see Aylward et al. 1996, for a contrary view). Larger third ventricle volumes, but no differences in prefrontal cortical, lateral ventricular, or intracranial volumes (Rosenberg et al., 1997). White matter reductions also reported (Jenike et al., 1996; *N*=20).

Sydenham's Chorea Increased sizes of the caudate, putamen, and globus pallidus, but not total cerebral, prefrontal, or midfrontal volumes (Giedd et al., 1996).

Multiple Sclerosis* Recurrent inflammatory lesions throughout the white matter; T2-hyperintense lesions most prominent in the corpus callosum, internal capsule, and around the lateral ventricular body and occipital horns (Lee et al., 1999). [*Unlike the above disorders, lesions alter image intensity rather than morphology; stereotaxic maps have revealed regional biases in lesion deposition (Narayanan et al., 1997; Lee et al., 1997).]

Demographic Factors

Age Cerebral volume declines by 2% per decade after age 50 (Miller et al., 1980). Corpus callosum area shows **g**reater age-related decline in males (Burke and Yeo, 1994; *N*=97). Large-scale morphometric studies of brain development include Giedd et al., 1996a,b (*N*=99,104); Paus et al., 1999 (*N*=111). Adolescent brain volume increases are specific to dorsal cortices (Jernigan et al., 1991; Pfefferbaum et al., 1994).

Gender 9% greater mean forebrain volume in adult men than women (*N*=71 men/49 women; Jäncke et al., 1997); controversy over whether splenium of *corpus callosum* is larger in women (DeLacoste-Utamsing and Holloway, 1982). In women, splenium may also be more bulbous (Clarke et al., 1989) or shaped differently (Davatzikos, 1996; Bookstein, 1997). For a review of this controversy, see Bishop and Wahlsten, 1997; Beaton, 1997; Thompson et al., 1999.

Handedness Normal left > right volume asymmetry of the *planum temporale* (PT) reduced in left-handers, without significant gender effects; same result in monozygotic twins discordant for handedness (Steinmetz, 1996). Hand preference associated with increased connectivity (increased neuropil in left area 4) and an increased intrasulcal surface of the precentral gyrus in the dominant hemisphere (Amunts et al., 1996).

.....